arXiv:1106.6232v1 [astro-ph.CO] 30 Jun 2011

June 30th 2011

Exploring the Low-Mass End of The $M_{\rm BH} - \sigma_*$ Relation with Active Galaxies

Ting Xiao[1], Aaron J. Barth[2], Jenny E. Greene[3], Luis C. Ho[4], Misty C. Bentz[5], Randi R. Ludwig[3] and Yanfei Jiang[6]

ABSTRACT

We present new measurements of stellar velocity dispersions, using spectra obtained with the Keck Echellette Spectrograph and Imager (ESI) and the Magellan Echellette (MagE), for 76 Seyfert 1 galaxies from the recent catalogue of Greene & Ho. These objects were selected from the Sloan Digital Sky Survey (SDSS) to have estimated black hole (BH) masses below $2 \times 10^6\ M_\odot$. Combining our results with previous ESI observations of similar objects, we obtain an expanded sample of 93 galaxies and examine the relation between BH mass and velocity dispersion (the $M_{\rm BH} - \sigma_*$ relation) for active galaxies with low BH masses. The low-mass active galaxies tend to follow the extrapolation of the $M_{\rm BH} - \sigma_*$ relation of inactive galaxies. Including results for active galaxies of higher BH mass from the literature, we find a zero point $\alpha = 7.68 \pm 0.08$ and slope of $\beta = 3.32 \pm 0.22$ for the $M_{\rm BH} - \sigma_*$ relation [in the form $\log M_{\rm BH} = \alpha + \beta \log(\sigma_*/200\ {\rm km\ s^{-1}})$], with intrinsic scatter of 0.46 ± 0.03 dex. This result is consistent, within the

[1]Key Laboratory for Research in Galaxies and Cosmology, Department of Astronomy, University of Science & Technology of China, Chinese Academy of Sciences, Hefei, Anhui 230026, China; xiaoting@mail.ustc.edu.cn.

[2]Department of Physics & Astronomy, University of California at Irvine, 4129 Frederick Reines Hall, Irvine, CA 92697-4575; barth@uci.edu.

[3]University of Texas at Austin, Department of Astronomy, 1 University Station, C1400, Austin, Texas 78712-0259, jgreene@astro.as.utexas.edu

[4]The Observatories of the Carnegie Institution for Science, 813 Santa Barbara Street, Pasadena, CA 91101; lho@obs.carnegiescience.edu.

[5]Department of Physics and Astronomy, Georgia State University, Astronomy Offices, One Park Place South SE, Suite 700, Atlanta, GA 30303, USA; bentz@chara.gsu.edu

[6]Department of Astrophysical Sciences, Princeton University, Princeton, NJ 08544, USA; yanfei@astro.princeton.edu

uncertainties, with the slope of the $M_{\rm BH} - \sigma_*$ relation for reverberation-mapped active galaxies with BH masses from 10^6 to 10^9 $M_\odot$. For the subset of our sample having morphological information from *Hubble Space Telescope* images, we examine the slope of the $M_{\rm BH} - \sigma_*$ relation separately for subsamples of barred and unbarred host galaxies, and find no significant evidence for a difference in slope. We do find a mild offset between low-inclination and high-inclination disk galaxies, such that more highly inclined galaxies tend to have larger σ_* at a given value of BH mass, presumably due to the contribution of disk rotation within the spectroscopic aperture. We also find that the velocity dispersion of the ionized gas, measured from narrow emission lines including [N II] λ6583 Å, [S II] $\lambda\lambda 6716, 6731$ ÅÅ, and the core of [O III] λ5007 Å (with the blue-shifted wing removed), trace the stellar velocity dispersion well for this large sample of low-mass Seyfert 1 galaxies.

Subject headings: galaxies: active — galaxies: dwarf — galaxies: nuclei — galaxies: Seyfert

1. Introduction

Dynamical studies of local galaxies over the past decade have firmly established that supermassive black holes (BHs) are present in most (possibly all) galaxies with massive bulges, and that the black hole mass tightly correlates with bulge mass and stellar velocity dispersion σ_* (Ferrarese & Merritt 2000; Gebhardt et al. 2000; Merritt & Ferrarese 2001; Tremaine et al. 2002; Marconi & Hunt 2003; Häring & Rix 2004; Gültekin et al. 2009). These correlations suggest coeval growth of the galaxy bulge and the central BH. The $M_{\rm BH} - \sigma_*$ relation is important both as a fundamental benchmark against which galaxy evolution models are tested (Haehnelt & Kauffmann 2000), and as a key input to calculations of the density of black holes in the Universe (Marconi et al. 2004; Volonteri et al. 2008).

The low-mass end of the mass function locally is where models of primordial BH seed formation show pronounced differences, thus improving the observational constraints on the low-mass end of the $M_{\rm BH} - \sigma_*$ relation can provide important constraints on the models. Theoretical work has proposed two types of seed models: "light seeds" (Madau & Rees 2001; Volonteri et al. 2003) formed as remnants of Population III stars, and "heavy seeds" (Koushiappas et al. 2004; Lodato & Natarajan 2006) from direct collapse of massive gas clouds in primordial halos. These different classes of models should result in different demographics for BHs in low-mass galaxies at the present epoch. Low-mass seeds lead to a

wide scatter in BH masses in low-dispersion galaxies (with some galaxies hosting very low-mass BHs) but a relatively high occupation fraction of BHs in low-mass galaxies, while in a heavy seed scenario, the BH occupation fraction is low but the minimum BH mass is larger (Volonteri et al. 2008; Volonteri & Natarajan 2009). Unfortunately, observations have not yet been sufficiently sensitive to distinguish between these scenarios, and additional observations to constrain the $M_{\rm BH} - \sigma_*$ relation at low masses are needed. Empirically, the slope and scatter of the $M_{\rm BH} - \sigma_*$ relation are still subject to debate, particularly at the low and high mass ends (Wyithe 2006). There is some recent work that suggests that the relation may be different for different types of host galaxies, i.e., for barred vs. unbarred galaxies, and for classical bulges vs. pseudo-bulges (Hu 2008; Graham & Li 2009; Gültekin et al. 2009; Greene et al. 2010). These differences may be more pronounced at lower masses and cause scatter in the overall $M_{\rm BH} - \sigma_*$ relation. However, due to the difficulty of obtaining direct stellar-dynamical measurements of BH masses in low-mass galaxies, much of the information on BH demographics at low mass comes from active galactic nuclei (AGNs). Recent *Hubble Space Telescope* (*HST*) imaging of low-mass Seyfert 1 galaxies selected from the SDSS by Greene & Ho (2004) also shows some evidence for a change in the $M_{\rm BH} - L_{\rm bulge}$ relation at low mass, probably indicative of a different mode of BH growth in these objects compared with higher-mass galaxies having classical bulges (Greene et al. 2008). In this paper, our goal is to expand the sample of low-mass AGNs having both black hole mass estimates from single-epoch spectroscopy and direct measurements of stellar velocity dispersion, in order to investigate the low-mass end of the $M_{\rm BH} - \sigma_*$ relation in more detail than was possible previously.

Greene & Ho (2004, 2007c, hereafter the GH07 sample) searched the SDSS database and presented a large sample of AGNs with low-mass BHs ($M_{\rm BH} < 2 \times 10^6 M_\odot$; see also Dong et al. 2007, for related work). The σ_* for the GH07 sample could not be determined from the SDSS spectra, because the instrumental resolution of ~ 70 km s^{-1} sets a practical lower limit to the σ_* that could be measured, and also because the S/N of the SDSS spectra was insufficient or the continuum was dominated by AGN emission rather than by starlight. Here we present new measurements of σ_* for objects in the GH07 sample. These new measurements provide a useful way to examine BH demographics, even if the individual BH masses are not highly accurate. In addition, our work provides a very large sample to examine relationships between gas and stellar kinematics for nearby AGNs. We present the sample properties, observations, and data reduction in Section 2, and measurements of σ_* and line-width in Section 3. We discuss the $M_{\rm BH} - \sigma_*$ relation in Section 4 and the narrow-line properties Section 5, with conclusions in Section 6.

2. Observations and Data Reduction

The objects observed at Keck and Magellan were selected from the sample of low-mass BHs presented by Greene & Ho (2007c). They selected 229 broad-line active galaxies with $M_{\rm BH} < 2 \times\ 10^6 M_\odot$ from SDSS DR4. They estimated the BH masses with the single-epoch virial method, using the Full Width Half Maximum (FWHM) and luminosity of the broad Hα emission line, following the methods first described by Greene & Ho (2005b). The virial calculation determines the radius of the broad-line region (BLR) using the radius-luminosity relationship of Bentz et al. (2006).

The objects were observed during 2008–2009 using the Echellette Spectrograph and Imager (ESI; Sheinis et al. 2002) at the Keck-II telescope and the Magellan Echellette (MagE; Marshall et al. 2008) Spectrograph at the Magellan II Clay telescope at Las Campanas Observatory. For each observation, the spectrograph slit was oriented at the parallactic angle. Flux standards and late-type giant stars (F4–M0) for use as velocity templates were observed during each night. Details of the Keck and Magellan observations and reductions are given below. We obtained useful data for 65 of 66 objects observed with MagE and for 13 objects observed with ESI; two objects were observed with both ESI and MagE. We also combine our new sample with the 17 similar objects previously presented by Barth et al. (2005, Hereafter BGH05). Including the BGH05 sample, our total sample consists of 93 low-mass SDSS AGNs.

ESI – Observations with ESI at Keck were made during the nights of 2008 March 1–2 UT. We used a $0\farcs75$ slit width, resulting in an instrumental dispersion of $\sigma_i \approx 22$ km s^{-1}. The spectra cover the wavelength range 3800–10900 Å across 10 echelle orders, and the dispersion is a constant 11.5 km s^{-1} pixel^{-1} in velocity. The exposure times for individual objects ranged from 900s to 3000s. One-dimensional spectra were extracted within a $1''$ extraction width, and wavelength- and flux-calibrated, with correction for telluric absorption bands, using standard techniques following the same methods we have previously used for ESI data (BGH05).

MagE – Observations with MagE at the Magellan II Clay telescope were carried out on the nights of 2008 April 9–13, 2008 August 28–30, and 2009 January 25–27 UT, using a $1''$ slit width, giving an instrumental dispersion of $\sigma_i \approx 26$ km s^{-1}, as measured from the arc lamp spectra. The spectral coverage is approximately 3200–10000 Å across 15 echelle orders, with a nearly constant dispersion of 23 km s^{-1} pixel^{-1}. Exposure times ranged from 1800–7200 s and were typically 5400 s. One-dimensional spectra were extracted from the CCD images and wavelength-calibrated using the `MAGE_REDUCE` package kindly provided by George Becker. The extraction width is typically $1\farcs5$ to $3''$. The `MAGE_REDUCE` package uses techniques for rectification and sky subtraction developed by Kelson (2003). Optimal

extractions (Horne 1986) were used for exposures of the bright stars, while for the galaxies a simple boxcar extraction was used in order to avoid spurious clipping of emission lines that can sometimes occur with optimal extractions. Flux calibration and telluric absorption correction were applied using the same methods used for the ESI data. Finally, cosmic rays were removed when combining multiple exposures.

Two objects, SDSS J093147.25+063503.2 and SDSS J131310.12+051942.1, were observed with both ESI and MagE, allowing a direct comparison of the spectra; see Figure 1. To facilitate comparison, the ESI data have been re-binned to the spectral resolution of the MagE data, and all the spectra have been re-scaled to have flux density of unity at 5100 Å. The Keck and Magellan spectra appear consistent across the entire available wavelength range, which illustrates the consistency of the flux calibration, except for differences in the emission lines, which are expected due to the difference in instrumental dispersion of the two instruments. For SDSS J093147.25+063503.2, the difference spectrum reveals significant residuals only in the peaks of the narrow emission lines, most likely resulting from the difference in instrumental dispersion. For SDSS J131310.12+051942.1, there is also evidence of some flux variation between the 2 observations. This could result from the different aperture size and different seeing between the two exposures, but could also be in part due to real variability of the continuum and broad emission lines. However, the time interval between these two observations is 329 days, and on such a short timescale the narrow lines probably would not be variable. Since there are residuals in the narrow lines in Figure 1 as well as the broad lines, the main cause is probably aperture size and seeing.

3. Measurements

3.1. Stellar Velocity Dispersions

The stellar velocity dispersions were measured by a direct fitting method (Burbidge et al. 1961; Rix & White 1992), in which the spectra of velocity template stars are broadened and fitted to the galaxy spectra locally in a specific spectral region. A Gaussian profile was assumed as the line-of-sight velocity distribution. We follow Barth et al. (2002) and Greene & Ho (2006a) and express the fitted model spectrum, $M(x)$, as

$$M(x) = \{[T(x) \otimes\ G(x)] + C(x)\}P(x), \tag{1}$$

where $T(x)$ is the stellar template spectrum, $G(x)$ is the Gaussian broadening function, $C(x)$ represents a featureless continuum, and $P(x)$ is a polynomial factor. Since our fits are performed across a small wavelength region, we adopt a quadratic polynomial for $C(x)$, which could also account for some other additive components, such as the "pseudo-continuum" due

to Fe II emission originating from BLR of AGN. The low-order multiplicative polynomial P allows for the differences between the template and the galaxy, including continuum shape, reddening in the galaxy spectrum, and wavelength-dependent flux calibration errors. We use a quadratic polynomial for P, since higher-order polynomials will tend to fit the absorption features and adversely affect the dispersion measurements (Barth et al. 2002). Besides the velocity dispersion and six parameters for these two polynomials, the redshift of the galaxy is also a free parameter. We determined the best-fit parameters by minimizing χ^2, using the Levenberg-Marquardt least-squares fitting routine provided by the `mpfit` package in IDL (Markwardt 2009).

Our collection of stellar templates includes 19 G and K giant stars observed with ESI and 22 F, G, K and M giant stars observed with MagE. For each galaxy, we inspect the fitting and discard the templates that fail to fit. Then we list the χ^2 of the remaining templates in ascending order, and select the first two-thirds to be well-fit templates. The measured velocity dispersion derived with the best-fitting template (minimum χ^2) is adopted to be the best estimate of σ_*. Generally, the best fits were obtained with K-giant templates. The uncertainty in measurement is calculated as the quadrature sum of the fitting uncertainty of the best-fit template and the standard deviation of the measurements of all the selected templates. A minimum of six templates are used in each calculation, except for several objects, marked by ":" behind the value of σ_* in Table 1, that were not well fit by six or more templates. In these cases, all the results of well-fit templates will be accounted in estimating the uncertainty.

The spectral region around the Ca II $\lambda\lambda 8498, 8542, 8662$ triplet ($\sim 8470 - 8700$ Å, hereafter the CaT region) is ideal for measuring velocity dispersions because the CaT lines are strong, not blended with other strong lines, and relatively insensitive to stellar population variations. They are also less strongly diluted by AGN continuum contamination than stellar features at blue wavelengths. However, for objects with redshift higher than 0.05, the CaT absorption features can be affected by both night sky emission residuals and telluric absorption bands, making it difficult to obtain useful measurements. Stellar features at bluer wavelengths are unaffected by telluric absorption, and we also carried out measurements in the Mg Ib region ($\sim 5050-5430$ Å) and the "Fe region" ($\sim 5250-5820$ Å) redward of Mg Ib for measurements, following Barth et al. (2002) and Greene & Ho (2006a). Greene & Ho (2006a) ran a series of simulations to evaluate the contamination of narrow emission lines, including [Fe VII] λ5158 Å, [Fe VI] λ5176 Å, and [N I] $\lambda\lambda 5197, 5200$ ÅÅ, around the Mg Ib features, as well as the pseudo-continuum of broad Fe II extending in this region. They found that the Fe region containing strong Fe I absorption features resulted in better recovery of σ_*, since it includes less contamination by coronal emission lines.

We tested these two regions by fitting stellar templates to a set of simulated spectra, composed as a linear combination of a K2 star, an A0 star, and a featureless linear continuum. The combined spectra were then broadened by a Gaussian velocity-broadening kernel with width ranging from $\sigma_* = 30$ to 100 km s^{-1} in increments of 10 km s^{-1}. Slight variations in the shape of the spectra, representing calibration errors and random errors, were imposed on the broadened model spectra, and the models were degraded to $S/N = 10$, 30, 50, and 100 per pixel. We also redshifted the model spectra by an arbitrary value comparable to the redshifts our observed sample. Then the modeled spectra were fitted using the methods described above, and the measured σ_* was compared with the input value. We find, for $\delta\sigma_* \equiv [\sigma(\text{output}) - \sigma(\text{input})]/\sigma(\text{input})$, that $\langle\delta\sigma_*\rangle = 0.02 \pm 0.11$ from the Mg Ib region and $\langle\delta\sigma_*\rangle = 0.03 \pm 0.02$ from the Fe region for $S/N = 30$, the median S/N for our observed sample. Reassuringly, the results from these test measurements are consistent with input values. We find that the scatter in results from the Mg Ib region is larger than that from Fe region. The scatter for both fitting regions decreases with increasing S/N, to 0.04 and 0.01 for $S/N = 100$, respectively. The larger scatter of the Mg Ib region might be attributed to template mismatch. We checked the template spectra and found that for different types of stars, the variations in the width of the Mg Ib lines are slightly larger than the width variations for the Fe I features. For different type of stars, for example, in the sequence of G8 $\rightarrow$ K3 $\rightarrow$ K5, the Mg Ib line widths increase, while Fe absorption widths are consistent; this may explain at least in part why the dispersion measurements obtained from the Mg Ib region have larger scatter.

In practice, when fitting to actual galaxy spectra, we excluded wavelength regions covering emission lines including [N I] $\lambda\lambda 5197, 5200$ ÅÅ and the high-ionization Fe lines. The majority of the objects have several high-ionization Fe lines, including [Fe VII] λ5158 Å, [Fe VI] λ5176 Å, [Fe VII] λ5278 Å, [Fe XIV] λ5303 Å and [Fe VI] λ5335 Å. We tested model fits that excluded and included the Mg Ib absorption features themselves, and found that the best-fit template could generally fit the Mg Ib features well for galaxies not dominated by AGN Fe emission. This is because most objects in this sample have relatively low σ_*, so the mismatch of [Mg/Fe] abundance ratio that sometimes affects template fits to elliptical galaxies with high σ_* (Worthey et al. 1992) is apparently not a significant issue for this sample.

In order to avoid issues of mismatch in flux calibration or spectral resolution across echelle orders, we prefer to measure velocity dispersions from a single echelle order (rather than from multiple orders that have been "stitched" together), and the specific fitting region for each individual galaxy was adjusted to remain within one echelle order. For MagE data, we first measured σ_* from both the Mg Ib region and the Fe region individually. We found that if these two regions are in the same order, we obtained highly consistent results from

both regions. This is partly due to the limited wavelength range of each order for MagE data and the fact that there is substantial overlap between the Mg I*b* and Fe regions. Therefore, if these two are on the same order for a given galaxy, we carry out a single fit extending across both of these regions, and list the result as σ_*(Mg I*b*) in Table 1. When a separate value is listed in the σ_*(Fe) column of the table, this denotes that the Mg I*b* and Fe regions fell in adjacent echelle orders and were fitted separately. Figure 2 illustrates some examples of both ESI and MagE spectra in the Fe and CaT regions.

We were able to obtain useful measurements of σ_* for 56 of the 76 newly observed galaxies. The two galaxies with both ESI and MagE observations have consistent velocity dispersions within the uncertainty measured by two instruments. The remaining 20 galaxies are either dominated by AGN emission or have S/N too low to permit a successful fit. We also re-measured σ_* for 15 of the 17 objects from BGH05 (excluding the two objects from that sample that were highly AGN-dominated). The results are consistent with the BGH05 measurements, within the uncertainties. If we define the deviation between our new measurements and BGH05 both from the Mg I*b* region, as $\Delta\sigma_* = \log\sigma_*(\mathrm{new}) - \log\sigma_*(\mathrm{BGH05})$, the mean value of $\Delta\sigma_*$ is less than 0.001 dex and the rms difference is only 0.02 dex. All of the σ_* measurements are summarized in Table 1. For the galaxies with more than one measurement of σ_* from different fitting regions, the corresponding results are mostly consistent within the uncertainties. We take the average of the available measurements as the best estimate of the stellar velocity dispersion in each object, and list as σ_* in Table 1.

3.2. Emission-line Properties

To decompose the Hα+[N II] lines, we first subtracted the underlying continuum. The continuum model is essentially the same as that in Equation 1 used to measure σ_*, but fitted over the spectral region surrounding Hα, covering the rest-frame region 6100–7100 Å. For this model spectrum ($M(x)$ in Equation 1), the velocity dispersion was constrained to lie within three times the 1σ uncertainties around the measured velocity dispersion as described in the preceding section. Emission lines were masked out from the calculation of χ^2 for the fits. The continuum fits were carried out on spectra in which the echelle orders were "stitched" together, since in some cases the Hα line falls near the end of an echelle order. The best-fit continuum model was then subtracted from the spectra to yield a pure emission-line spectrum.

We used multiple-Gaussian models to fit the Hα and [N II] lines as well as [S II] $\lambda\lambda 6717, 6731$ ÅÅ. We followed Greene & Ho (2007b), using a multi-component Gaussian fit to the [S II] doublet to model other blended lines. Up to 4 Gaussians were used to model

the [S II] doublet. The velocities and widths of the two [S II] lines were constrained to be the same, while the intensity ratio was allowed to vary. For objects with very weak or absent [S II] emission, we used the core of the [O III] λ5007 Å line as the narrow-line model instead.

The [N II] doublet lines were constrained to have their relative rest-frame wavelengths and intensity ratio fixed to their laboratory values of 35.42 Å and 2.96, respectively. We then fit as many Gaussian components to the broad component of Hα as needed to achieve an acceptable fit: starting with a single Gaussian model, new components were added one at a time if they resulted in 20% decrease in χ^2. Generally, one or two Gaussians proved sufficient to fit the broad Hα emission adequately. Figure 3 shows some examples of fits to Hα. Only a small number of galaxies with asymmetric profiles or very broad wings required a third Gaussian component. In most cases we were able to achieve an acceptable fit to the Hα+[N II] blend, but there are a few cases ($\sim$ 6) for which no acceptable fit to the narrow Hα line could be obtained with the [S II] model. For those cases, we relaxed the width constrains on the narrow lines. In each case, the width of the narrow Hα in the best-fit model remained quite close to the [S II] line width but the Hα fit was significantly improved by allowing its width to be a free parameter.

We also modeled the Hβ + [O III] region in continuum-subtracted spectra, in the rest-frame range of 4800-5150 Å, following procedures similar to those described above for the Hα+[N II] region. We used double-Gaussian models for the broad component of Hβ as well as for [O III], for which the double Gaussians represent a wing and a core component. The corresponding components in the two [O III] lines are constrained to have the same velocity width, and the wavelength separations and intensity ratios are fixed at their laboratory values. For those galaxies with significant broad Fe II emission (mainly Fe II $\lambda\lambda$4924, 5018 ÅÅ), we adopted an analytical model for the broad Lorentzian system "L1" in Véron-Cetty et al. (2004, see their Appendix A). Each Fe II line was fitted with a Lorentzian profile, allowing the line center to vary within a small range around the expected value to account for shifting from the systemic redshift. The widths of both Fe II lines were constrained to be the same, while their flux ratio was allowed to vary. In order to model the narrow Hβ, we follow Greene & Ho (2005b) to use the profile of [S II]. The Hβ centroid was fixed to the relative wavelength of narrow Hα if necessary, and its flux was limited to be no larger than the value for Case B recombination (Hα = 3.1Hβ, Osterbrock & Ferland 1989). The procedure produced acceptable fit to Hβ in most cases, except for some objects ($\sim$ 13) in which the profile of [S II] seems not be a good model for narrow Hβ, possibly resulting from small changes in spectral resolution across different echelle orders of the spectra. In these cases we used a single Gaussian to model narrow Hβ, and we relaxed the width and flux constraints. In Figure 3 we show some examples of best-fit models for the Hβ + [O III] region. Individual components for Fe II emission are also shown if they are present. It turns

out that the detected Fe II lines in this sample are relatively narrow, typically 700 km s^{-1} FWHM, significantly narrower than the commonly used Fe II template I ZW 1, whose broad line system "L1" has FWHM = 1100 km s^{-1} (Véron-Cetty et al. 2004).

The FWHM of the overall profile of broad Hα is used for tracing the velocity dispersion of gas in the BLR, in the close environment of the black hole. We continue to use the FWHM(Hα) as a measurement of the line width for the whole sample in a consistent way, because the commonly used Hβ lines suffer from low S/N. Broad Hβ is often weak and sometimes not even detectable for objects in our sample.

To estimate errors on the line width measurements, we should include statistical uncertainties from profile fits caused by noise and other random errors from spectral extraction and calibration, and uncertainties in continuum subtraction and deblending of broad components from narrow emission lines. In general, the formal fitting uncertainties from the profile fits are quite small, typically only 11 km s^{-1}. Since the broad lines for this low-mass sample are narrow (mostly with FWHM < 2000 km s^{-1}), the measurements of widths are much less affected by continuum subtraction than broad-lined AGN (see Section 2.5 of Dong et al. 2008). Due to the small wavelength range over which the continuum-subtraction fits were performed and the good quality of the fits, the continuum subtraction does not add substantially to the error budget for the line widths. To explore the uncertainty from the emission-line profile deblending in more detail, we create a set of artificial spectra from the best-fit model, following Greene & Ho (2005b). For each galaxy, we created a realization of the combined emission lines from the best-fit model parameters, and added Gaussian noise to match the S/N of the data. The artificial spectra created this way suffer from the same deblending difficulty as the original data. Then the artificial spectra are fitted with multiple-Gaussian models using the fitting procedure described above. The difference between the model and measured FWHM(Hα) is typically $\sim$ 5% (or 0.02 dex). With these artificial spectra, we also investigated the uncertainty associated with the choice of model for the narrow-line profile, which often dominates the uncertainty in the decomposition of narrow/broad lines. We substituted the narrow-line model with the [S II] profile, the core of [O III], and narrow Hβ respectively, in the fitting procedure with the multiple-Gaussian model above. The typical standard deviation in the FWHM of broad Hα is $\sim$ 8% (or 0.03 dex). These two sources of error are combined to be typically $\sim$ 9% (or 0.04 dex), and taken as the estimated uncertainty of FWHM(Hα).

3.3. Comparison of Broad-Line Widths With GH07

It is instructive to compare our broad Hα measurements with those obtained from SDSS spectra by GH07. The smaller spectroscopic apertures for the Keck and Magellan data result in a smaller degree of starlight dilution of the AGN features, and the higher spectral resolution of the new data should permit more accurate deblending of the emission lines. Thus, we expect that the Keck and Magellan data should generally yield more accurate measurements of the broad Hα widths, particularly for very weak Hα emission lines. The SDSS spectra, on the other hand, have a more reliable flux calibration. In a small fraction of the objects from the GH07 sample, the broad Hα emission in the SDSS spectra is so weak that it is uncertain whether a distinct broad component is genuinely present or not, and our new spectra are particularly useful for testing the reality of these features tentatively seen in the SDSS data.

We examined how our new measurements of the broad Hα FWHM compare with the results that GH07 obtained from fitting SDSS spectra, to test whether the objects with very weak broad Hα in GH07's low-mass AGN sample were genuine Seyfert 1 galaxies or not. We visually inspected the best-fit models for all the objects and divided them into two categories: objects with "definite" and "possible" broad Hα. In the following we refer to the two sub-categories as the d and p sub-samples, as indicated in Table 1. For the d sample, the wings of broad Hα generally extend beyond the [N II] emission lines, and the broad Hα is significantly wider than the narrow emission lines such as [N II]. We classified objects as belonging to the p subsample if the peak amplitude of broad Hα was less than twice the RMS pixel-to-pixel deviation in the continuum-subtracted spectrum in the region surrounding Hα, or if the ratio of the flux of broad Hα to the RMS deviation of the continuum-subtracted spectrum was below 200. Some examples of "possible" broad Hα are shown in Figure 4.

Among the 93 galaxies in our sample, 14 (15%, 1 galaxy observed both by ESI and MagE) had ambiguous "possible" broad Hα emission. To investigate whether this was simply due to these 15 spectra having low S/N, we examined the average S/N in the Hα+ [N II] region, and found that only three p objects had very low S/N of < 11. Overall, the objects classified as being in the p category have a median S/N of 25, compared to a median value of 40 for our whole sample, so some of the p objects may simply be suffering from low S/N. However, some of the p objects have very high S/N spectra, so we can not attribute all the cases of ambiguity in broad Hα to low S/N. There are six p objects which only show very weak or possible broad Hα in the SDSS spectra (these are denoted as the c subsample in GH07). The other 8 out of the 14 p galaxies are classified as broad-line AGNs by GH07. The difference between the SDSS results and our new fitting results could possibly be due to intrinsic AGN variability or variable AGN obscuration. Among the eight p galaxies,

SDSS J093147.25+063503.2 is confirmed to have outflow components in the narrow lines, which might have mimicked part of the broad component in SDSS spectra. There are also five galaxies in the c ("candidate") sample of GH07 which we now classify as having definite broad Hα based on our new high-resolution spectra. A likely explanation is that the better quality of our new spectra makes the decompositions more accurate and better reveals the intrinsic properties of the broad components. Therefore, eight (9%) out of 82 galaxies previously classified as broad-line AGNs by GH07 are found to have only possible broad Hα from the high-resolution spectra. This indicates the likely rate of false positive detections of broad Hα in the SDSS sample for objects near the threshold of detectability for broad Hα. In our sample, there is one object, SDSS J145045.54−014752.8, showing obvious double-peaked features in narrow lines, and also a definite broad component in Hα (see the last object of the right panel in Figure 3).

We compare our new measurements of broad Hα FHWM to those of GH07 by defining $\Delta\mathrm{FWHM} \equiv \log \mathrm{FWHM(H}\alpha)_{\mathrm{new}} - \log \mathrm{FWHM(H}\alpha)_{\mathrm{GH07}}$. Figure 5 displays ΔFWHM vs. $\mathrm{FWHM(H}\alpha)_{\mathrm{new}}$. These two measurements are in reasonable agreement up to FWHM $\sim$ 1000 km s^{-1}, but the difference increases as FWHM increases beyond 1000 km s^{-1}. This is probably because the higher resolution of the new data enables us to fit the emission lines more accurately with more complex multi-Gaussian models, although some of the difference may be due to intrinsic source variability as well.

4. Black Hole Masses and the $M_{\mathrm{BH}} - \sigma_*$ Relation

In this section we discuss our method of estimating black hole masses, and investigate the $M_{\mathrm{BH}} - \sigma_*$relation for our sample. In the following formulae for M_{BH} estimation, L_{5100} denotes the AGN continuum luminosity $\lambda \mathrm{L}_\lambda$ at $\lambda = 5100$ Å.

4.1. Black Hole Mass

The black hole mass is estimated via the virial relationship, $M_{\mathrm{BH}} = f R_{\mathrm{BLR}} \Delta V^2 / G$, where R_{BLR} is the radius of the BLR, and the orbital velocity at that radius is estimated by the velocity width of the broad emission line, ΔV. Assuming that the gas in the BLR is virialized, the gas velocity traces the central mass in AGN, which is dominated by the black hole within the BLR radius.

The broad line width can be measured with the FWHM or σ_{line}, which is the second moment of the profile, or the line dispersion. Both have merits and difficulties (Peterson et al.

2004). The line dispersion $\sigma_{\rm line}$ has been suggested to be a more robust and precise estimator of viral velocity when measured from the RMS spectra of reverberation mapping datasets (Peterson et al. 2004; Collin et al. 2006). However, it is highly sensitive to the contribution from the extended line wings, and therefore less robust in single-epoch spectra when there is blending of other emission lines on the line wings (Denney et al. 2009). For measurements from single-epoch data, the FWHM is more commonly adopted (see a review in McGill et al. 2008); it is sensitive to the line core and to the decomposition of the broad and narrow components, but it is relatively insensitive to the accuracy of measurement of faint extended wings on the broad-line profile. Denney et al. suggests that when the S/N is lower than $10-20$, both line width measurements would become unreliable, and line-profile fits would introduce systematic errors to single-epoch masses (e.g., ~ 0.17 dex offset in $M_{\rm BH}$ estimated with FWHM, their Table 5). In practice, we generally fit the broad Hα with two Gaussians. This is a purely empirical procedure and no specific physical meaning is assigned to the two components separately. Thus, we measure FWHM(Hα) from the overall profile of the Gaussian components used to fit the broad component of Hα.

We follow GH07's approach (see Greene & Ho 2007c, Appendix) to calculate $M_{\rm BH}$, which is estimated by using the line-width of Hα and the BLR radius inferred from the broad Hα luminosity (Greene & Ho 2005b). In this work, the width of the broad Hα emission line is measured by decomposing the Hα+[N II] lines in the ESI and MagE data. The method relies on the broad-line region radius-luminosity ($R_{\rm BLR}-L$) relation derived from reverberation mapping (Kaspi et al. 2005; Bentz et al. 2006, 2009) to determine the BLR radius from the estimated continuum luminosity, which in turn is estimated from the broad Hα luminosity following Greene & Ho (2007c) since this is more accurately determined than the nonstellar continuum from our spectroscopic data. We update GH07's "recipe" for determining BH masses with the revised $R_{\rm BLR}-L$ relation presented by Bentz et al. (2009), who analyzed high-resolution *HST* images of 34 reverberation-mapped (RM) AGNs to obtain more accurate measurements of AGN continuum luminosity. The revised $R_{\rm BLR}-L$ relation from Bentz et al. (2009) is

$$\log\left(\frac{R_{\rm BLR}}{\text{lt-days}}\right) = 1.50^{+0.05}_{-0.02} + 0.519^{+0.063}_{-0.066}\log\left(\frac{L_{5100}}{10^{44}\ \text{ergs s}^{-1}}\right), \quad (2)$$

We follow GH07 in assuming $f = 0.75$ (Netzer 1990) although we note that this f value is not derived for any specific physical model of the BLR. The choice of this particular f factor aids in comparison of our results with prior work, as described below. From Greene & Ho (2005b), the empirical relation between the line widths of broad Hα and Hβ is

$$\mathrm{FWHM(H}\beta) = (1.07 \pm 0.07) \times 10^3 \left(\frac{\mathrm{FWHM(H}\alpha)}{10^3 \text{ km s}^{-1}}\right)^{1.03\pm0.03} \text{ km s}^{-1}. \quad (3)$$

Combining these results with the virial relationship gives the BH mass as

$$\log\left(\frac{M_{\rm BH}}{M_\odot}\right) = 6.72^{+0.08}_{-0.06} + 0.519^{+0.063}_{-0.066} \log\left(\frac{L_{5100}}{10^{44} \text{ ergs s}^{-1}}\right) + (2.06\pm0.06) \log\left(\frac{\mathrm{FWHM(H}\alpha)}{10^3 \text{ km s}^{-1}}\right). \quad (4)$$

If we substitute the continuum luminosity with luminosity of Hα using the following empirical relation from Greene & Ho (2005b),

$$L_{\rm H\alpha} = (5.25 \pm 0.02) \times 10^{42} \left(\frac{L_{5100}}{10^{44} \text{ ergs s}^{-1}}\right)^{1.157\pm0.005} \text{ ergs s}^{-1}, \quad (5)$$

then we obtain the BH mass as

$$\log\left(\frac{M_{\rm BH}}{M_\odot}\right) = 6.40^{+0.09}_{-0.07} + (0.45\pm0.05) \log\left(\frac{L_{\rm H\alpha}}{10^{42} \text{ ergs s}^{-1}}\right) + (2.06\pm0.06) \log\left(\frac{\mathrm{FWHM(H}\alpha)}{10^3 \text{ km s}^{-1}}\right). \quad (6)$$

Our Keck and Magellan spectra were not all taken under photometric conditions, and since the observations were obtained through narrow spectroscopic apertures, slit losses can be significant. The SDSS spectra have a more consistent flux calibration, so it is preferable to use $L(\mathrm{H}\alpha)$ measured from the SDSS data, even if this does introduce some additional uncertainty due to the fact that the Hα linewidths and luminosities are measured from non-simultaneous observations. Most objects in our sample are in the GH07 sample of active galaxies containing low-mass BHs, so we can obtain $L_{\rm H\alpha}$ for most of our sample from GH07. For the 5 objects in BGH05 sample that were not included in GH07, we use the Hα luminosity $L_{\rm H\alpha}$ from Greene & Ho (2004). One object in the BGH05 sample was not part of either the GH07 or Greene & Ho (2004) catalogs, and for this object we estimated $L_{\rm H\alpha}$ from the L_{5100} measured by Barth et al. (2005) using the $L_{\rm H\alpha}$-L_{5100} relation (Equation 5) of Greene & Ho (2005b).

The BH masses estimated by Equation 6 are systematically lower by 0.08 dex than those obtained using the method described in the Appendix of Greene & Ho (2007c), since they used the earlier version of the $R_{\rm BLR} - L$ relationship from Bentz et al. (2006). We still refer to our mass estimator as $M_{\rm GH07}$, since it follows their basic method with only the $R_{\rm BLR} - L$

relationship updated. The RMS scatter in the $L_{\rm H\alpha}$-L_{5100} relation is ~ 0.2 dex (Greene & Ho 2005b). If we take the uncertainties on the Hα luminosity as discussed in Greene & Ho (2005b), which are typically 0.13 dex, the typical formal uncertainties on the BH masses are 0.14 dex based on propagation of the measurement errors on the Hα luminosity and width. This random error does not include the important systematic uncertainty in the normalization factor f. This is comparable to the observable error for BH masses in Seyfert galaxies ($0.12 - 0.16$ dex) estimated by Denney et al. (2009) based on single-epoch data, considering the effects of AGN variability and random measurement errors.

In the discussion above, we followed GH07 and updated their recipe to calculate $M_{\rm BH}$. The method is based on the Hα emission lines only (not requiring a continuum measurement) and it allows us to compare our results in a consistent way with previous work on SDSS AGNs presented by GH07. One particular point to consider is that our mass estimates assume a normalization factor $f = 0.75$ for the virial masses, for consistency with GH07 and other previous work, but this is not a unique choice for f. The virial factor has been the subject of much discussion in the literature (e.g. Onken et al. 2004; Collin et al. 2006), and different f values have been used in various recipes to obtain $M_{\rm BH}$ estimates. McGill et al. (2008) compared $M_{\rm BH}$ estimators based on different emission-line and continuum measurements and showed that systematic errors could be as large as 0.38 ± 0.05 dex.

We would like to examine how different recipes change the $M_{\rm BH}$ values of our sample and the $M_{\rm BH} - \sigma_*$ relation that will be discussed in Section 4.2. Most of the recipes make use of continuum luminosity, but we lack direct measurements of the optical AGN continuum luminosity for our sample. An alternative way is to substitute L_{5100} with the broad Hα luminosity using the empirical relationship given by Greene & Ho (2005b). Some recipes rely on measurements of FWHM(Hβ), and to test those relationships we substitute FWHM(Hβ) with FWHM(Hα) using the empirical relationship between Hα and Hβ widths from Greene & Ho (2005b). If we use the recipe of Vestergaard & Peterson (2006), the masses would be higher by about 0.25 dex. The formalism presented by Wang et al. (2009) gives relatively larger BH mass than our estimator in the low mass end, typically about 0.6 dex higher at BH mass of $\langle \log M_{\rm GH07}/M_\odot \rangle = 6$. They calibrated their BH mass estimator by fitting the reverberation-based masses for 35 AGNs using the continuum luminosity and Hβ FWHM, as $\log(M_{\rm BH}/M_\odot) = \alpha + \gamma \log(L_{5100}/10^{42}\ {\rm ergs\ s^{-1}}) + \beta \log({\rm FWHM(H}\beta)/10^3\ {\rm km\ s^{-1}})$ and fixed γ to be 0.5. Their fits yield values of $\alpha = 1.39$ and $\beta = 1.09$. This value of β is less than $\beta = 2$, which is commonly adopted for mass estimators. The 35 RM AGNs used in their fits mostly have BH masses in the range from $10^7\ M_\odot$ to $10^9\ M_\odot$, and α tends to compensate for the mass difference in the fitting. This results in larger BH masses in the low mass range, i.e., for objects below about $10^7\ M_\odot$.

There is some lower limit to the BH masses that we are able to detect in SDSS data, due to a combination of factors. A possibly low BH occupation fraction in very low-mass galaxies would result in a low detection rate. The low luminosity of AGNs with small black holes makes the AGNs hard to detect. The host galaxy has to be bright enough to be spectroscopically targeted by SDSS, and the S/N of SDSS spectra is limited. Moreover, the large aperture of SDSS spectra can mix AGN emission with H II regions and dilute the AGN signal. Since we have identified the "definite" broad-lined AGNs that have genuine broad Hα in our sample, we obtain a cleaner sample that illustrates how low we can really go in selecting objects with low $M_{\rm BH}$ using SDSS. Our definite broad-lined sample with successful measurements of σ_* has a median BH mass $\langle M_{\rm BH}\rangle = 9.5 \times 10^5 M_\odot$, and a minimum of $2 \times 10^5 M_\odot$.

4.2. $M_{\rm BH} - \sigma_*$ Relation

Figure 6 shows the $M_{\rm BH} - \sigma_*$ relation for our sample of AGNs with low BH masses, and for active galaxies with higher black hole masses as well as nearby galaxies with direct dynamical measurements. The comparison sample of 56 active galaxies with higher BH masses based on single-epoch spectroscopy were selected from SDSS DR3 with $z \leq 0.05$ by Greene & Ho (2006b, hereafter GH06 sample), but the $M_{\rm BH}$ values have been re-calculated with our updated mass recipe (Equation 6). Literature data on 24 RM AGNs with stellar velocity dispersion measurements presented by Woo et al. (2010, and the references therein) were included. The $M_{\rm BH}$ for these RM AGNs were calculated from the virial products (VPs) listed in Table 2 of Woo et al. (2010). Since $\sigma_{\rm line}$ was used in VP, an isotropic velocity distribution gives $f_\sigma = 3$, assuming σ_{line} = FWHM/2 (Onken et al. 2004); The ratio between FWHM and $\sigma_{\rm line}$ is different for different line profiles, i.e. FWHM/$\sigma_{line} = 2.35$ for a Gaussian profile, and it varies around an average of 2 (Collin et al. 2006). Instead of the virial factor f obtained by Woo et al., we assume $f_\sigma = 3$ for consistency with the GH07 sample. This would decrease the masses by 0.24 dex compared to those listed in their work. We also included the well-known intermediate-mass BHs in NGC 4395 with reverberation mass $M_{\rm BH} = (3.6\pm1.1)\times 10^5 M_\odot$ (Peterson et al. 2005) and the velocity dispersion with an upper limit $\sigma_* \leq 30$ km s^{-1} from Filippenko & Ho (2003), and POX 52 with virial mass $M_{\rm BH} \approx (3.1-4.2)\times 10^5 M_\odot$ based on broad Hβ line width and L_{5100} (Barth et al. 2004; Thornton et al. 2008) and velocity dispersion $\sigma_* = 36 \pm 5$ km s^{-1} from Barth et al. (2004). Masses for both objects were calculated utilizing the virial coefficient $\langle f_\sigma\rangle = 5.5$ (Onken et al. 2004; Peterson et al. 2004), we also scaled down both masses by 0.26 dex for consistency with other objects shown on the plot. Note that the virial normalization factor we assumed is arbitrary, and the derived $M_{\rm BH}$ was decreased by about 0.26 dex compared to masses derived using the f factor from

Onken et al. (2004). But the slope of $M_{\rm BH} - \sigma_*$ relation is independent of f. Our low-mass sample appears to smoothly follow the extension of the $M_{\rm BH}-\sigma_*$ relation for inactive galaxies, and there seems to be no strong change in slope across the whole mass range including active and inactive galaxies. We will quantify the slope for all the active galaxies described above.

Assuming a log-linear form $\log M_{\rm BH} = \alpha + \beta \log(\sigma_*/200 \text{ km s}^{-1})$, we fit the slope and zero point of the $M_{\rm BH} - \sigma_*$ relation for all the active galaxies with two regression methods: the symmetric least-squares fitting method, *fitexy* (Press et al. 1992) modified following Tremaine et al. (2002), and the maximum-likelihood estimate (MLE) method *linmix_err* (Kelly 2007), both implemented in IDL. The former method accounts for uncertainties in both coordinates as well as the intrinsic scatter by adding a constant to the error in the dependent variable, and solves for the best linear fit by minimizing the reduced χ^2 to unity. *Linmix_err* uses a Bayesian method to account for measurement errors and intrinsic scatter, and computes a posterior probability distribution function of parameters. Since there is no significant difference between the results from the two regression methods, we will only quote results from the MLE method *linmix_err*. We obtain $\alpha = 7.68 \pm 0.08$ and $\beta = 3.32 \pm 0.22$, with $\epsilon_0 = 0.46 \pm 0.03$ dex. The slope is a bit flatter than that for nearby galaxies, which have $\beta = 4.24 \pm 0.41$ (Gültekin et al. 2009), but consistent with Greene & Ho (2006b) and Woo et al. (2010) who both showed evidence of a shallower slope for active galaxies than the inactive $M_{\rm BH} - \sigma_*$ relation. If we fix the slope β to the best-fit value of 4.24 for nearby galaxies, we obtain, for the full sample of active galaxies, a zeropoint of $\alpha = 7.99 \pm 0.04$, which is -0.13 ± 0.09 offset from the value of $\alpha = 8.12 \pm 0.08$ from Gültekin et al. (2009).

We now consider residuals in the $M_{\rm BH}-\sigma_*$ relation, defined as $\Delta M_{\rm BH} \equiv \log(M_{\rm BH}/M_\odot) - \log(M_{\rm BH}/M_\odot)_{\rm fit}$, where $\log(M_{\rm BH}/M_\odot)_{\rm fit}$ is calculated from σ_*, as a function of the bolometric luminosity and Eddington ratio (Figure 7). We follow GH07's method for bolometric correction to estimate the bolometric luminosity from $L_{\rm H\alpha}$, according to $L_{\rm bol} = 2.34 \times 10^{44} (L_{\rm H\alpha}/10^{42})^{0.86}$ ergs s^{-1}. Among the 93 objects in our sample, the median value of the Eddington ratio is $\langle L_{\rm bol}/L_{\rm Edd} \rangle = 0.3$, where $L_{\rm Edd} \equiv 1.26 \times 10^{38} (M_{\rm BH}/M_\odot)$. The sample is dominated by objects radiating at substantial fractions of their Eddington limits, since the SDSS selection favors identification of the most luminous AGNs in any mass range. We find that the residual $\Delta M_{\rm BH}$ is significantly correlated with $L_{\rm bol}$ (Figure 7a). The Spearman rank correlation coefficient is $r_s = 0.33$, with a probability $P < 10^{-3}$ that no correlation is present. Moreover, $\Delta M_{\rm BH}$ shows a strong anti-correlation with $L_{\rm bol}/L_{\rm Edd}$ (Figure 7b, $r_s = -0.53$, $P < 10^{-9}$). We are wary to overinterpret these correlations, since the $L_{\rm bol}/L_{\rm Edd}$ is formally anti-correlated with $M_{\rm BH}$ and $M_{\rm BH}$ is correlated with $L_{\rm bol}$ because both of them are deduced based on $L_{\rm H\alpha}$.

Note that for our $M_{\rm BH}$ estimates we are using propagated measurement uncertainties

based on the errors in Hα width and luminosity, while the true uncertainties in $M_{\rm BH}$ are probably dominated by the uncertainty in the BLR geometry and the chosen value of f. If we adopt 3σ uncertainties in $M_{\rm BH}$ as measurement errors and do the regression again, there is little change in either the slope or zero point of the derived $M_{\rm BH} - \sigma_*$ relation, but the intrinsic scatters decrease by about 35% to $\epsilon_0 = 0.28 \pm 0.05$ dex. The regression parameters for different samples and different uncertainties considered are listed in Table 2. Woo et al. (2010) recently reported the $M_{\rm BH} - \sigma_*$ relation for 24 RM active galaxies with BH mass $10^6 < M_{\rm BH}/M_\odot < 10^9$. They obtained a slope $\beta = 3.55 \pm 0.60$ and intrinsic scatter $\epsilon_0 = 0.43 \pm 0.08$, which are also consistent with our result. In the following, we will examine whether the intrinsic scatter varies as a function of mass.

We divide the active galaxies mentioned above into two data sets, with lower and higher $M_{\rm BH}$, and analyze the intrinsic scatter ϵ_0 for the two data sets. The lower-$M_{\rm BH}$ data set includes our sample and the Lick AGN Monitoring Project (LAMP) sample presented by Woo et al. (2010). The higher-$M_{\rm BH}$ data set includes GH06 SDSS sample and 17 previous RM active galaxies (collected also in Woo et al. (2010)). Assuming that the $M_{\rm BH}$ recipe we used is equally valid at all masses (which is not necessarily the case), we fit the two data sets and quantify the intrinsic scatter to be $\epsilon_0 = 0.38 \pm 0.04$ dex for the low-$M_{\rm BH}$ sample presented here and $\epsilon_0 = 0.40 \pm 0.04$ dex for the higher-$M_{\rm BH}$ objects. The scatter for low-mass data set slightly changes when including NGC 4395 and POX 52, or excluding the LAMP sample. The scatter decreases a little to $\epsilon_0 = 0.34 \pm 0.04$ dex if we exclude the "possible" broad Hα objects. The derived scatters for the two data sets are consistent, indicating that the intrinsic scatter in virial BH masses is not strongly mass-dependent. We also examine the standard deviation of residuals from the best-fit $M_{\rm BH} - \sigma_*$ relation for the two data sets, and get 0.50 dex and 0.44 dex for the low and high mass range, respectively.

The intrinsic scatter in $M_{\rm BH} - \sigma_*$ across the entire mass range is about 0.46 dex, corresponding to a factor of ~ 3. That is close to the intrinsic scatter for inactive galaxies, $\epsilon_0 = 0.44 \pm 0.06$ (Gültekin et al. 2009). We will show in §4.5 that the intrinsic scatter persists or even increases if we scale the active galaxies to follow the $M_{\rm BH} - \sigma_*$ relation of nearby galaxies with direct measurements of BH masses and then fit the relation for the combined sample of the active galaxies and nearby galaxies. Some of the dispersion in the $M_{\rm BH} - \sigma_*$ relation may result from different galaxy morphological types following different $M_{\rm BH} - \sigma_*$ loci, as recent evidence has suggested (Hu 2008; Greene et al. 2008; Graham & Li 2009; Gültekin et al. 2009; Gadotti & Kauffmann 2009; Greene et al. 2010). For example, the intrinsic scatter in $M_{\rm BH} - \sigma_*$ relation of early-type galaxies (referring to elliptical galaxies and S0 galaxies) is smaller than for late-type galaxies (Graham 2008; Gültekin et al. 2009). There is tentative evidence for a similar trend in the Greene & Ho (2004) sample, whose host galaxy morphologies have been investigated by Greene et al. (2008) using *HST* images. The

difference could either be due to unaccounted systematic error in the $M_{\rm BH}$ measurements for spirals, or because the scatter in $M_{\rm BH}$ for spirals is actually larger, as might happen if the behavior of BHs hosted by pseudobulges (see Kormendy & Kennicutt 2004, for a review) and classical bulges are different. This has been suggested by Hu (2008), who found that pseudobulges tend to host lower $M_{\rm BH}$ than classical bulges at a given σ_*. Similarly, a recent study by Greene et al. (2010) presents stellar velocity dispersions for a sample of nine megamaser disk galaxies with accurately measured BH masses in the range of $\sim 10^7$ $M_\odot$. They find that the maser galaxies fall below the $M_{\rm BH} - \sigma_*$ relation of elliptical galaxies defined by Gültekin et al. (2009). Based on morphology and stellar population properties, they speculate that most of the nine megamaser galaxies are likely to contain pseudobulges, providing further support for the idea that the pseudobulge $M_{\rm BH} - \sigma_*$ relation is offset below the relation for classical bulges (Hu 2008; Gadotti & Kauffmann 2009). In §4.3 below, we investigate the possible dependence of the $M_{\rm BH} - \sigma_*$ relation fit on host galaxy morphological type for our sample.

Simulations of massive BH growth indicates that the scatter in the $M_{\rm BH} - \sigma_*$ relation should increase toward the low-mass end. In models with high-mass seeds, galaxies evolve from well above the present-day $M_{\rm BH} - \sigma_*$ relation toward the relation, while galaxies starting with low-mass seeds first lie far below the relation and their BHs grow to move toward the relation (Volonteri 2010, and references therein). Furthermore, Volonteri (2010) suggested that for heavy seeds of $\sim 10^5$ $M_\odot$, the low-mass end of the $M_{\rm BH} - \sigma_*$ relation will flatten to an asymptotic value. In our sample, we do not find clear evidence for increasing scatter in the $M_{\rm BH} - \sigma_*$ relation at low masses, and we can not discriminate among possible seed models based on our sample. Increasing scatter at the low-mass end should nevertheless be a generic result regardless of the seed masses or the details of the BH growth mechanism. As discussed by Peng (2007), major mergers decrease the scatter of the $M_{\rm BH}$-$M_{\rm gal}$ relation because of a central-limit tendency of the BH-to-galaxy mass relation to eventually converge to some mean value.

Given the previous expectation that low-mass galaxies should show a larger scatter in the $M_{\rm BH} - \sigma_*$ relation than high-mass galaxies, as well as the recent observational suggestions of an offset $M_{\rm BH} - \sigma_*$ relation for pseudobulges relative to classical bulges, it remains somewhat puzzling that the Type 1 AGN samples do not show an obvious trend of either increasing scatter or changes in slope toward lower masses. This appears to be the case both for the small sample of AGNs with reverberation mapping (Woo et al. 2010), and for the larger sample of objects with single-epoch masses presented here. It could be that the random errors on individual AGN virial BH mass estimates are so large that the scatter in the mass estimates (resulting from variations in BLR kinematics, inclination, or other properties) simply dominates over the intrinsic scatter in the $M_{\rm BH} - \sigma_*$ relation for these ob-

jects, preventing us from detecting mass-dependent variations in the intrinsic scatter. Direct stellar-dynamical measurements of BH masses in nearby RM AGNs can be an important cross-check on the derived masses. However, while observations so far do not reveal evidence for any dramatic offsets between stellar-dynamical and reverberation masses, only a few objects are presently amenable to both types of measurements (Davies et al. 2006; Onken et al. 2007; Hicks & Malkan 2008). For the vast majority of reverberation-mapped AGNs, the angular size of the BH's gravitational sphere of influence is too small to be resolved by either *HST* or by ground-based telescopes employing adaptive optics, and only a small number of broad-lined AGNs are currently suitable targets for stellar-dynamical measurements of $M_{\rm BH}$.

4.3. Morphology: Barred versus Unbarred Disk Galaxies

Recent work by Graham et al. (2011) has suggested that the $M_{\rm BH} - \sigma_*$ relation is different for AGNs with different host galaxy morphological types (i.e. barred disks or unbarred disks). For our sample, we can carry out a preliminary check for any offsets in the $M_{\rm BH} - \sigma_*$ plane as a function of host morphology. The SDSS images are not sufficient to carry out a full census of host galaxy types for this sample, but there is morphological information for a subset of our sample from an *HST* Wide Field Planetary Camera2 (WFPC2) imaging snapshot survey with the F814W filter (Jiang et al. 2011). Among the galaxies in our sample having *HST* images, there are 38 objects which are morphologically classified as disk galaxies and which also have $M_{\rm BH}$ and velocity dispersion measurements, including 12 barred and 26 unbarred galaxies. Only one galaxy from the GH06 higher-mass SDSS sample is included in the *HST* imaging survey; it is classified as an unbarred disk galaxy. Including the reverberation-mapped AGN sample compiled by Woo et al. (2010), as well as NGC 4395, and LAMP objects, we have morphological information for a total of 63 disk galaxy AGN hosts (25 barred and 38 unbarred). The morphological classifications for the reverberation-mapped objects are from NED where available, and otherwise adopted from classification by Bentz et al. (2009), while the classification for LAMP objects are provided by Bentz et al. (2011, in preparation). If we remove the galaxies with a "possible" broad Hα component, there are 56 disk galaxies with morphological information (22 barred and 34 unbarred). One caveat in our division is that it is based on optical images, while it has been suggested that some galaxies appear to be unbarred in optical bands, but are very clearly barred when viewed in the infrared (e.g. Block & Wainscoat 1991; Mulchaey & Regan 1997). Despite this caveat, we are limited by the data presently available and we carry out a preliminary examination based on the optical host-galaxy morphologies.

We re-do the regression fits for the $M_{\rm BH} - \sigma_*$ relation as in §4.2 for different subsamples,

and the results are listed in Table 3. The best fit of the $M_{\rm BH} - \sigma_*$ relation for the full subsample of disk galaxies ($\alpha = 7.50 \pm 0.13$, $\beta = 3.04 \pm 0.30$) is consistent with that for the entire sample of active galaxies described previously ($\alpha = 7.68 \pm 0.08$, $\beta = 3.32 \pm 0.22$). Within the uncertainties, the slope is consistent with the slope of 4.05 ± 0.83 for 24 nonellipticals reported by Gültekin et al. (2009). Fixing the slope to 4.05 yields an intercept of $\alpha = 7.89 \pm 0.06$, which also agrees well with $\alpha = 8.01 \pm 0.16$ for nonellipticals (Gültekin et al. 2009). The fit for barred disks only gives $\alpha = 7.81 \pm 0.27$ and $\beta = 4.13 \pm 0.72$, similar to the $M_{\rm BH} - \sigma_*$ relation ($\alpha = 7.80 \pm 0.10$, $\beta = 4.34 \pm 0.56$) for barred inactive galaxies presented by Graham et al. (2011).

Figure 8 shows the morphological type for the disk galaxies on the $M_{\rm BH} - \sigma_*$ plot, and also the best fits of the $M_{\rm BH} - \sigma_*$ relations for barred and unbarred disks (see Table 3). We consider our most reliable results to come from the subset of our sample that excludes the p objects with uncertain detections of broad Hα. For this subsample, we find $\alpha = 7.80 \pm 0.29$ for barred disks versus 7.52 ± 0.15 for unbarred disks, and the slope $\beta = 4.03 \pm 0.80$ for barred disks versus 3.01 ± 0.33 for the unbarred subset. Thus, the barred disks have a marginally larger zeropoint and steeper slope than unbarred disks, but the difference is not significant given the substantial uncertainties on the fits. We also fit the $M_{\rm BH} - \sigma_*$ relation with the slope fixed to that of inactive galaxies, 4.24 (Gültekin et al. 2009), as an additional test for any offset. With fixed slope, the distinction between the barred and unbarred subsamples almost vanishes (see Table 3). Alternatively, if we were to adopt the high slope value proposed by Graham et al. (2011) ($\beta = 5.13$), then the zeropoints would be all increased by about 0.35.

4.4. Disk Inclination

We have measured σ_* for our sample from the ESI and MagE spectra obtained with slit widths of $0\farcs75$ and $1''$, respectively. At the median redshift ($\langle z \rangle = 0.08$, or luminosity distance D_L=300 Mpc) for our sample, $1''$ corresponds to a scale of 1.5 kpc. If the bulge is not the dominant component of the host galaxy over that scale, then the slit spectra will be contaminated by the light from the disk, and the measured σ_* will include contributions from the rotational velocity of stars orbiting on the disk. Specifically, σ_* will be increased artificially in an edge-on disk, and might be slightly decreased in a face-on disk. In order to examine the effect of disk inclination on our sample, we use the axis ratio b/a to indicate inclination, where b/a close to 1 implies a face-on (low-inclination) system and b/a close to 0 denotes an edge-on (high-inclination) system. The disk axis ratio is obtained from fits to *HST* images. For the subset of our sample having *HST* imaging, the axis ratio measurements are based on the analysis of the WFPC2 snapshot imaging survey data (Jiang et al. 2011).

For reverberation-mapped AGNs, axis ratios measured from *HST* imaging data are taken from Bentz et al. (2009, their Table 4) and from Bentz et al. (2011, in preparation). We divide the sample into three axis-ratio bins: $b/a > 0.88$, $0.72 < b/a < 0.88$, and $b/a < 0.72$.

Figure 9 shows the disk galaxies compiled in §4.3 in the $M_{\rm BH} - \sigma_*$ plot, labeled by axis ratio. The low-inclination objects (large blue triangles) lie apparently to the left of the medium- (large orange squares) and high-inclination (large red circles) objects. We define $\Delta M_{\rm BH}$ as the $M_{\rm BH}$ deviation from the best-fit $M_{\rm BH} - \sigma_*$ relation reported by Gültekin et al. (2009). The distributions of $\Delta M_{\rm BH}$ for the three bins are shown in Figure 10. A K-S test on the distributions of $\Delta M_{\rm BH}$ for the low- and high-inclination subsamples yields a probability of 0.011, indicating that the distribution of the offset $\Delta M_{\rm BH}$ is likely to be significantly different for these two subsamples. Two extra PG objects (PG 1229+204 & PG2130+099) with $M_{\rm BH}$ and σ_* measurements are also shown on Figure 9. Their axis ratios of disk components are 0.62 and 0.55, respectively, and they are classified as high-inclination objects. Including these two objects in the K-S test above does not alter the result. We also carry out fits to $M_{\rm BH} - \sigma_*$ relation for each subsample, and list the best-fit parameters in Table 4. With the slope fixed to 4.24, the low-inclination subsample shows offsets from the other two subsamples by more than 0.4 dex. This gives additional evidence that the low-inclination and high-inclination systems are significantly offset in the $M_{\rm BH} - \sigma_*$ plane, such that the more highly inclined host galaxies tend to have higher σ_* at a given value of $M_{\rm BH}$. The offset is consistent with the expectation that disk rotation contributes more significantly to the measured values of σ_* in the more highly inclined systems. This may be one source of error contributing to the scatter in the relation, and it may also introduce a bias to the zeropoint of the relation. Although it would be preferable to plot an $M_{\rm BH} - \sigma_*$ relation that did not include this possible bias, there is no simple way to correct for the rotational contribution to the velocity dispersions from our data.

4.5. Virial Normalization Factor

In the discussions above, we have adopted an arbitrary virial factor $f = 0.75$ for consistency with most previous work on the SDSS-selected GH07 sample. Alternatively, we can also fit for the value of f that brings our sample into the best agreement with the local $M_{\rm BH} - \sigma_*$ relation, following the same method used by Onken et al. (2004) and Woo et al. (2010) for reverberation-mapped AGNs. The values reported by Gültekin et al. (2009) are $\alpha = 8.12 \pm 0.08$ and $\beta = 4.24 \pm 0.41$. Fixing the slope to 4.24 for our full sample, we obtain $\alpha = 7.99 \pm 0.04$ for $f = 0.75$ as presented in §4.2. Therefore, the mean virial factor determined from this fit would be $\langle f \rangle = 1.01 \pm 0.21$. Alternatively, fitting our sample to the

$M_{\rm BH} - \sigma_*$ relation from Graham et al. (2011) would give a lower value of $\langle f \rangle = 0.52 \pm 0.08$. If we take the subsample of the 15 low-inclination galaxies above in §4.4 and scale to the $M_{\rm BH} - \sigma_*$ relation from Gültekin et al., we get $\langle f \rangle = 0.56 \pm 0.17$. These results are reasonably compatible with previous calibrations of $\langle f \rangle$ for reverberation-mapped AGNs, taking into account the fact that our work uses the FWHM as the measure of line width while the reverberation-based mass scale is based on the second moment of the Hβ line (e.g., Onken et al. 2004; Woo et al. 2010). Fundamentally, the calibration of $\langle f \rangle$ via the $M_{\rm BH} - \sigma_*$ relation is still limited by small-number statistics, and improving the determination of the virial normalization factor will require increasing the number of AGNs having high-quality reverberation mapping data as well as the number of spiral galaxies having direct measurements of $M_{\rm BH}$ from spatially resolved dynamics, and equally important, obtaining accurate σ_* measurements for them.

For completeness of our analysis, we fit the $M_{\rm BH} - \sigma_*$ relation for the combined sample of active and nearby galaxies. First we use the virial factor derived above to recompute the BH masses for the active galaxies. Then we re-do the regression fit for the combined sample. Using the virial factor $\langle f \rangle = 1.01$ derived above, which is based on normalizing the AGNs to the $M_{\rm BH} - \sigma_*$ relation of Gültekin et al., we combine the AGNs with the 49 nearby galaxies with direct dynamical measurements of BH masses presented by the same authors. Then the regression for the combined sample yields $\alpha = 8.02 \pm 0.05$ and $\beta = 3.81 \pm 0.16$ with an intrinsic scatter of $\epsilon_0 = 0.46 \pm 0.03$. If the alternative $\langle f \rangle = 0.52$ is used, then the fit yields a zero point of 7.89 ± 0.06 and a slope of 4.14 ± 0.16 with an intrinsic scatter of 0.49 ± 0.03.[1] The intrinsic scatter for the combined sample is the same as or even larger than that for active galaxies only. We note that the slope and the intrinsic scatter depend on how we select the virial factor, because the active galaxies are scaled to the local $M_{\rm BH} - \sigma_*$ relation first and then included for the fit.

[1] Instead we could choose $\langle f \rangle = 0.52$ based on normalizing the AGNs to the $M_{\rm BH} - \sigma_*$ relation of Graham et al. (2011), and then combine the AGNs with the 64 galaxies with direct BH mass measurements listed by Graham et al. Assigning a 10 percent error to the σ_* for the 64 galaxies as Graham et al. suggested, the regression for the combined sample yields $\alpha = 7.93 \pm 0.05$ and $\beta = 4.30 \pm 0.16$ with $\epsilon_0 = 0.48 \pm 0.03$. Assigning a 5 percent error to the σ_* instead will yield almost the same results.

5. Narrow Emission-line Properties

5.1. Stellar vs. Gas Velocity Dispersion

It is well-known that the velocity dispersion of the ionized gas in the narrow-line region (NLR), most often measured from the [O III] λ5007 Å line, correlates with the stellar velocity dispersion of the host galaxy bulge, suggesting that gravity dominates the global kinematics of the NLR for active galaxies (e.g. Whittle 1985; Nelson & Whittle 1996; Boroson 2003; Greene & Ho 2005a; Bian et al. 2006; Komossa & Xu 2007; Barth et al. 2008). The high-resolution ESI and MagE data provides an opportunity to examine this relationship in galaxies of small σ_*. In addition to the [O III] line, we also consider lines from lower ionization species such as [N II] λ6583 Å and the [S II] $\lambda\lambda 6716, 6731$ ÅÅ doublet, and check their relationship to σ_* for our sample.

For the [O III] $\lambda\lambda 4959, 5007$ ÅÅ lines, each was fitted by a double-Gaussian model, representing a core and often (but not always) a blueshifted wing component. Generally the core component has a higher peak flux than the wing component. In some cases, the two-component model sometimes over-fits noise fluctuations near the line peak, resulting in individual Gaussian components with very narrow widths. We set an empirical criterion for the separation of the two components (> 80 km s^{-1}) to define the blue- and red-shifts. The blue- or red-shifted wing component was removed from the FWHM$_{core}$ measurements if the separation was > 80 km s^{-1}. For the other cases, where the centroids of the two components were separated by less than 80 km s^{-1}, we measured the FWHM from the [O III] profile and took the resulting value to be FWHM$_{core}$. Detailed studies of some galaxies where the NLR is spatially resolved reveal the possibility that the entire [O III] line may be outflowing (Fischer et al. 2011, and references therein). We use the relative velocity of the narrow component of Hβ to help determine the core component, since the Balmer recombination lines are less affected by the outflow when present.

Figure 11 illustrates the relationships between FWHM([O III])/2.35 and σ_* for the core and wing components of the [O III] line as well as for the entire [O III] profile (Figure 11c). The FWHM of the [O III] core correlates with σ_*, with a Spearman rank correlation coefficient $r_s = 0.61$, and a probability $P_{\rm null}$ less than 10^{-4} for the null hypothesis of no correlation (Figure 11a). The relationship between the FWHM of the entire [O III] profile and σ_* has a larger scatter, consistent with previous results (e.g. Nelson & Whittle 1996; Greene & Ho 2005a; Barth et al. 2008). This illustrates that if we use the FWHM of [O III] as a proxy for σ_* in active galaxies, the high-velocity wing component should be removed from the profile. The velocity shifts between the centroids of the wing to core components, defined as ΔVel, are mainly negative (Figure 12, left panel), representing blue-shifts of the wing components,

while the centroid velocity of the core components are generally close to the systemic velocity measured from the stellar absorption lines. If the blue-shifted wing component of [O III] is driven by winds or outflows (Whittle 1985; Komossa et al. 2008), then the strength or velocity offset of the wing component could correlate with some measure of AGN activity, such as the Eddington luminosity ratio, $L_{\rm bol}/L_{\rm Edd}$. Thus we investigate how the equivalent width (EW) ratio of the [O III] wing to core components correlates with Eddington ratio, but we find no correlation between them. We find that ΔVel correlates with $L_{\rm bol}/L_{\rm Edd}$ only weakly ($r_s = -0.24$, Figure 12, middle panel). We also find that ΔVel correlates well with the FWHM of the wing component ($r_s = 0.56, P_{null} < 0.001$) and less strongly with the FWHM of the core component ($r_s = 0.41, P_{null} = 0.03$). This confirms that the previously established correlation between [O III] blueshift and line width continues to hold in this low-mass regime.

We also examine the correlation between gas and stellar velocity dispersions for the [S II] doublet and the [N II] λ6583 Å emission line, which has been decomposed from broad Hα. Since we use the [S II] profile as the model for the narrow lines for most cases (discussed in Section 3.2), we can use either the [S II] or [N II] lines. The [N II] line is adopted here because there are a few cases for which [S II] is too weak to measure its width reliably. The FWHM is measured from the overall, combined profile of gaussians fitted to each narrow emission line. As shown in Figure 11, the FWHM of [N II] correlates well with σ_*, with a Spearman rank correlation coefficient $r_s = 0.72$ and $P_{null} < 10^{-4}$. We follow Ho (2009) to define the gaseous velocity dispersion $\sigma_g \equiv$ FWHM/2.35 and the residual of $\sigma_g - \sigma_*$ to be $\Delta\sigma \equiv \log\sigma_g - \log\sigma_*$. While Ho (2009) finds a correlation between $\Delta\sigma$ and Eddington ratio for nearby active galaxies, we do not see such a correlation in our sample (Figure 12, right panel). Our sample mostly lies below the relation found by Ho (2009), but is generally consistent with Greene & Ho (2005a). The objects scatter around $\Delta\sigma = 0$ ($\sigma_g = \sigma_*$), regardless of increasing Eddington ratio.

5.2. Emission-line Diagnostics

We have measured emission lines of Hβ, [O III] λ5007 Å, Hα, [N II] λ6583 Å, and [S II] $\lambda\lambda$6716, 6731 ÅÅ, which enable us to plot our sample on line-ratio diagnostic diagrams (e.g. BPT diagrams; **?**Veilleux & Osterbrock 1987), as shown in Figure 13, and to compare our measurements with the SDSS measurements obtained with larger spectroscopic apertures (fiber diameter of 3″). The flux of [O I] λ6300 Å was also measured from the starlight-subtracted spectra by fitting with a single Gaussian. From the new data (with aperture sizes of 0.″75 × 1.″0 and 1.″× (1.″5 ∼ 3″) for the ESI and MagE data, respectively), we see that

a few objects move out of the H II region of the BPT diagrams and into the Seyfert region above the maximum starburst line (Kewley et al. 2006). With the small-aperture data, most objects lie in the Seyfert region of the diagram, with some objects extending to relatively low values of [N II]/Hα which are indicative of metallicity lower than typical for classical Seyferts (Groves et al. 2006).

We investigate whether the line ratios measured from the small-aperture spectra systematically change relative to measurements based on the SDSS spectra. The distributions of line ratios are shown on the top and right panels in Figure 5.2. These distributions for the low-ionization ratios [N II]/Hα, [S II]/Hα, and [O I]/Hα only change slightly as a function of aperture size, with systematic offsets less than 0.08 dex between the median values for the small-aperture and SDSS measurements. This could be the effect of various parameters, due to the complex NLR conditions, including metallicity, ionization parameter, electron density, and dust reddening. But the [O III]/Hβ ratio measured from the small-aperture data is systematically 0.3 dex higher than the values measured from the SDSS fiber aperture. The simplest interpretation is that in the larger SDSS aperture the emission lines included a larger contribution of emission from H II regions, which would have lower [O III]/Hβ than the AGNs. This would also imply that the host galaxies are actively star-forming, and we may be witnessing growth of the host galaxy bulge or pseudobulge coevally with the BH growth. Integral-field observations at high angular resolution would be particularly useful for examining the distribution and luminosity of H II regions in the host galaxies.

These line-ratio diagrams are generally used to discriminate between star-forming galaxies and AGNs (e.g. Ho et al. 1997; Kauffmann et al. 2003; Hao et al. 2005; Barth et al. 2008). However, as noted by GH07, the broad-line AGNs do not lie exclusively above the maximum starburst line of Kewley et al. on the BPT diagrams, and some objects even fall below the empirical line of Kauffmann et al. (2003) in the region of pure star-forming galaxies. That is, judging by the narrow-line ratios alone, these objects would not be classified as AGNs. For these objects, the detection of the broad Hα emission is the primary clue that an AGN is present, and if the broad emission lines were obscured by a dusty parsec-scale torus or by dust lanes in the host galaxy then these objects would not have been identified as AGNs at all.

We explore whether the objects which fall below the maximum starburst line are unusual in terms of any of the measured parameters including σ_*, σ_{gas} (indicated as FWHM([N II])/2.35), the flux ratio between [O III] wing and core, the Fe II strength (relative to [O III]), FWHM(Hα), or the flux ratio between the narrow and broad components of Hα ($F_{n/b}$). We find that this sub-population of objects does not exhibit any unusual properties in terms of these parameters, except in $F_{n/b}$, which shows a higher relative strength of the narrow

components in this sub-population. Further investigation shows the median redshift of the sub-population ($z \sim 0.1$) is larger than the whole sample ($z \sim 0.08$). Thus the higher $F_{n/b}$ ratio could be explained by the dilution of extended star formation contained in the aperture. It is unfortunately difficult to derive any detailed information on the stellar populations of the hosts from the spectra because of the strong AGN contribution to the spectra. We examined the ESI and MagE spectra, finding that higher-order Balmer absorption of significant strength is visually apparent in 18 objects (about 20% of the sample), of which about 10 objects are in the sub-population below the maximum starburst line. The absorption features imply contributions from A stars. Thus, compared with the sample as a whole, a larger fraction of objects in the H II sub-population appear to have significant contributions from intermediate-age stellar populations.

6. Conclusions

We have obtained new echelle spectroscopy of 76 Seyfert 1 galaxies selected to have low-mass black holes based on their broad-line widths and $L_{\rm H\alpha}$ luminosity, and we obtain reliable measurements of σ_* for 56 galaxies. Including the previous 17 Seyfert galaxies presented by Barth et al. (2005), our low-mass AGN sample consists of 93 galaxies, of which 71 have measured velocity dispersions. The velocity dispersion ranges from 31 to 138 km s^{-1}, and the data tend to lie on the extrapolation of the $M_{\rm BH} - \sigma_*$ relation of inactive galaxies. We find that the intrinsic scatter in virial $M_{\rm BH} - \sigma_*$ relation is not strongly mass-dependent. Combining our results with 56 SDSS active galaxies (Greene & Ho 2006a) and reverberation-mapped AGNs from the literature with σ_* measurements and $M_{\rm BH}$ estimation, as well as the two well-known intermediate-mass BHs in NGC 4395 and POX 52, we carry out new fits to the $M_{\rm BH} - \sigma_*$ relation, finding a zero point of $\alpha = 7.68 \pm 0.08$ and slope $\beta = 3.32 \pm 0.22$ for the $M_{\rm BH} - \sigma_*$ relation in the form of $\log M_{\rm BH} = \alpha + \beta \log(\sigma_*/200{\rm km\ s^{-1}})$, for an assumed virial normalization factor of $f = 0.75$. The AGN $M_{\rm BH} - \sigma_*$ relation has an intrinsic scatter of 0.46 ± 0.03 dex, comparable to the intrinsic scatter of the $M_{\rm BH} - \sigma_*$ relation observed for inactive galaxies. Among our low-mass BH sample with definite broad Hα components, we find that the lower limit of BH masses detectable in this SDSS sample is $2 \times 10^5 M_\odot$ (for $f = 0.75$). We do not find a significant offset or slope difference in the $M_{\rm BH} - \sigma_*$ relation between the subsamples of barred and unbarred disk galaxies. We do find that the disk galaxies with high inclination angles (edge-on systems) show a mild offset from the face-on systems in the $M_{\rm BH} - \sigma_*$ relation. The rotation of the disk in the edge-on systems may artificially increase the measured σ_*, which may partly introduce a scatter in the relation. We also confirm that the narrow emission lines [N II] λ6583 Å, [S II] $\lambda\lambda$6716, 6731 ÅÅ, and the core of [O III] λ5007 Å (with the blue-shifted wing removed) have velocity dispersions

which trace the stellar velocity dispersion well, confirming that the forbidden emission-line widths can be used as a useful proxy for the stellar velocity dispersion in low-mass AGNs.

We thank the anonymous referee for comments and suggestions that helped to improve the manuscript. We are grateful to Virginia Trimble, Tinggui Wang, and Xiaobo Dong for advice and discussions during the course of this work, George Becker for his reduction package (`MAGE_REDUCE`) for MagE echelle spectra, and Thomas Matheson for helpful discussion on flux calibration. T.X. acknowledges support from the Chinese Scholarship Council during her visit at UC Irvine, where main part of this work was carried out. Research by A.J.B. was supported by NSF grant AST-0548198. Some of the data presented herein were obtained at the W.M. Keck Observatory, which is operated as a scientific partnership among the California Institute of Technology, the University of California and the National Aeronautics and Space Administration. The Observatory was made possible by the generous financial support of the W.M. Keck Foundation. The authors wish to recognize and acknowledge the very significant cultural role and reverence that the summit of Mauna Kea has always had within the indigenous Hawaiian community. We are most fortunate to have the opportunity to conduct observations from this mountain. Funding for the SDSS has been provided by the Alfred P. Sloan Foundation, the Participating Institutions, the National Science Foundation, the U.S. Department of Energy, the National Aeronautics and Space Administration, the Japanese Monbukagakusho, the Max Planck Society, and the Higher Education Funding Council for England. The SDSS Web Site is http://www.sdss.org/. This research has made use of the NASA/IPAC Extragalactic Database (NED) which is operated by the Jet Propulsion Laboratory, California Institute of Technology, under contract with the National Aeronautics and Space Administration.

REFERENCES

Barth, A. J., Greene, J. E., & Ho, L. C. 2005, ApJ, 619, L151

———-. 2008, ApJ, 136, 1179

Barth, A. J., Ho, L. C., Rutledge, R. E., & Sargent, W. L. W. 2004, ApJ, 607, 90

Barth, A. J., Ho, L. C., & Sargent, W. W. 2002, ApJ, 124, 2607

Bentz, M. C., et al. 2011, in preparation

Bentz, M. C., Peterson, B. M., Netzer, H., Pogge, R. W., & Vestergaard, M. 2009, ApJ, 697, 160

Bentz, M. C., Peterson, B. M., Pogge, R. W., Vestergaard, M.,& Onken, C. A. 2006, ApJ, 644, 133

Bian, W., Yuan, Q., & Zhao, Y. 2006, MNRAS, 367, 860

Block, D. L., & Wainscoat, R. J. 1991, Nature, 353, 48

Boroson T. A. 2003, ApJ, 585, 647

Burbidge, E. M., Burbidge, G. R., & Fish, R. A. 1961, ApJ, 133, 393

Collin, S., Kawaguchi, T., Peterson, B. M. & Vestergaard, M. 2006, A&A, 456, 75

Dasyra, K. M., et al. 2007, ApJ, 657, 102

Davies, R. I., et al. 2006, ApJ, 646, 754

Denney, K. D., Peterson, B. M., Dietrich, M., Vestergaard, M., & Bentz, M. C. 2009, ApJ, 692, 246

Dong, X.-B., et al. 2007, The Central Engine of Active Galactic Nuclei, Ed. by Ho, L. C. & Wang, J.-M., ASP Conference Series, Vol. 373, p57

Dong, X.-B., Wang, T.-G., Wang, J.-G., Yuan, W.-M., Zhou, H.-Y., Dai, H.-F., & Zhang, K. 2008, MNRAS, 383, 581

Ferrarese, L., & Merritt, D. 2001, ApJ, 539, 9

Filippenko, A. V., & Ho, L. C. 2003, ApJ, 588, L13

Fischer, T. C., Crenshaw, D. M., Kraemer, S. B., Schmitt, H. R., Mushotsky, R. F., & Dunn, J. P. 2011, ApJ, 727, 71

Gadotti, D. A., & Kauffmann, G. 2009, MNRAS, 399, 621

Gebhardt, K., et al. 2000, AJ, 119, 1157

Graham, A. W. 2008, ApJ, 680, 143

Graham, A. W., & Li, I. H. 2009, MNRAS, 698, 812

Graham, A. W., Onken, C. A., Athanassoula, E., & Combes, F. 2011, MNRAS, 412, 2211

Grier, C. J., et al. 2008, ApJ, 688, 837

Greene, J. E., & Ho, L. C. 2004, ApJ, 610, 722

———-. 2005a, ApJ, 627, 721

———-. 2005b, ApJ, 630, 122

———-. 2006a, ApJ, 641, 117

———-. 2006b, ApJ, 641, L21

———-. 2007a, ApJ, 656, 84

———-. 2007b, ApJ, 667, 131

———-. 2007c, ApJ, 670, 92

Greene, J. E., Ho, L. C., & Barth, A. J. 2008, 688, 159

Greene, J. E., et al. 2010, ApJ, 721, 26

Groves, B., Heckman, T., & Kauffmann, G. 2006, MNRAS, 371, 1559

Gültekin, K., et al. 2009, ApJ, 698, 198

Haehnelt, M. G., & Kauffmann, G. 2000, MNRAS, 318, L35

Hao, L., et al. 2005, AJ, 129, 1783

Häring, N., & Rix, H. W. 2004, ApJ, 604, L89

Hicks, E. K. S., & Malkan, M. A. 2008, ApJS, 174, 31

Ho, L. C. 2009, ApJ, 699, 638

Ho, L. C., Filippenko, A. V., & Sargent, W. L. W. 1997, ApJS, 112, 315

Horne, K. 1986, PASP, 98, 617

Hu, J. 2008, MNRAS, 386, 2242

Jiang, Y. F., Greene, J. E., Ho, L. C., Xiao, T., & Barth, A. J. 2011, ApJ, submitted

Kaspi, S., Maoz, D., Netzer, H., Peterson, B. M., Vestergaard, M., & Jannuzi, B. T. 2005, ApJ, 629, 61

Kauffmann, G., et al. 2003, 346, 1055

Kelly, B. C. 2007, ApJ, 665, 1489

Kelson D. D. 2003, PASP, 115, 688

Kewley L. J., Groves, B., Kauffmann, G., & Heckman, T. 2006, MNRAS, 372, 961

Komossa, S., & Xu, D. 2007, ApJ, 667, L33

Komossa, S., Xu, D., Zhou, H., Storchi-Bergmann, T., & Binette, L. 2008, ApJ, 680, 926

Kormendy, J., & Kennicutt, R. C. Jr 2004, ARA&A, 42, 603

Koushiappas S. M., Bullock, J. S., & Dekel, A. 2004, MNRAS, 354, 292

Lodato, G., & Natarajan, P. 2006, MNRAS, 371, 1813

Madau, P., & Rees, M. J. 2001, ApJ, 551, L27

Marconi, A., & Hunt, L. K. 2003, ApJ, 589, L21

Marconi, A., et al. 2004, MNRAS, 351, 169

Markwardt, C. B. 2009, Astronomical Society of the Pacific Conference Series, 411, 251

Marshall, J. L., et al. 2008, *Astronomical Telescope*, Proc. SPIE, 7014, 701454

McGill, K. L., Woo, J. H., Treu, T., Matthew, A. M. 2008, 673, 703

McLure, R. J., & Dunlop, J. S. 2004, MNRAS, 352, 1390

Merritt, D., & Ferrarese, L. 2001, ApJ, 547, 140

Mulchaey, J., & Regan, M. W. 1997, ApJ, 482, 135

Nelson, C. H., & Whittle, M. 1996, ApJ, 465, 96

Netzer, H. 1990, in Active Galactic Nuclei, ed., T. J.-L. Courvoisier & M. Mayor (Berlin: Springer), 57

Onken, C. A.; Ferrarese, L.; Merritt, D.; Peterson, B. M.; Pogge, R. W.; Vestergaard, M.; Wandel, A. 2004, ApJ, 615, 645

Onken, C. A., et al. 2007, ApJ, 670, 105

Osterbrock, D. E.; Ferland, G. J. 1989, Astrophysics of Gaseous Nebulae and Active Galatic Nuclei (University Scinece Books)

Peng, C. Y. 2007, ApJ, 671, 1098

Peterson, B. M., et al. 2004, ApJ, 612, 682

Peterson, B. M., et al. 2005, ApJ, 632, 799

Press, W. H., Teukolsky, S. A., Vetterling, W. T., & Flannery, B. P. 1992, Numerical Recipes in C (2nd ed; Cambridge: Cambridge Univ. Press)

Rix, H.-W., & White, S. D. M. 1992, MNRAS, 254, 389

Sheinis, A. I., Bolte, M., Epps, H. W., Kibrick, R. I., Miller, J. S., Radovan, M. V., Bigelow, B. C., & Sutin, B. M. 2002, PASP, 114, 851

Thorton, C. E., Barth, A. J., Ho, L. C., Rutledge, E. R., & Greene, J. E. 2008, ApJ, 686, 892

Tremaine, S., et al. 2002, ApJ, 572, 740

Treu, T., Woo, J. H., Malkan, M. A., & Blandford, R. D. 2007, ApJ, 667, 117

Veilleux, S., & Osterbrock, D. E. 1987, ApJS, 63, 295

Véron-Cetty, M. P., Joly, M., Véron P. 2004, A&A, 417, 515

Vestergaard, M., & Peterson, B. M. 2006, ApJ, 641, 689

Volonteri, M., Haardt, F., & Madau, P. 2003, ApJ, 582, 559

Volonteri, M., Lodato, G., & Natarajan, P. 2008, MNRAS, 383, 1079

Volonteri, M., & Natarajan, P. 2009, MNRAS, 400, 1911

Volonteri, M. 2010, to appear in The Astronomy and Astrophysics Review

Wang, J.-G., et al. 2009, ApJ, 707, 1334

Whittle, M. 1985, MNRAS, 213, 1

Woo, J.-H., et al. 2010, ApJ, 716, 269

Worthey, G., Faber, S. M., & Gonzalez, J. J. 1992, ApJ, 398, 69

Wyithe, J. S. B. 2006, MNRAS, 365, 1082

This preprint was prepared with the AAS LaTeX macros v5.2.

Table 1. Observations and Measurements

SDSS Name	Flag	z	Exp. (s)	S/N	σ(Mg Ib) (km s^{-1})	σ(Fe) (km s^{-1})	σ(Ca II) (km s^{-1})	σ_* (km s^{-1})	FWHM(Hα) GH07	FWHM(Hα) (km s^{-1})	log $L_{\rm H\alpha}$	log($M_{\rm BH}$)	Obs.
SDSS J000111.15−100155.5		0.0493	5400	38	71 ± 3	···	82 ± 6	76 ± 3	1870	1660	40.11	6.00	m
SDSS J002228.36−005830.6		0.1059	5400	35	54 ± 5 :	60 ± 5	···	57 ± 4	807	620	41.37	5.69	m
SDSS J004042.10−110957.6		0.0277	3600	26	57 ± 5	55 ± 6	55 ± 5	55 ± 3	1530	2380	39.67	6.13	m
SDSS J010712.03+140844.9	gh01	0.0771	2982	16	38 ± 4	39 ± 5	38 ± 9	38 ± 4	914	874	41.44	6.03	b
SDSS J011749.81−100114.5		0.1411	5400	37	···	···	···	···	756	640	41.53	5.79	m
SDSS J012055.92−084945.4	p	0.1246	5400	14	55 ± 6	51 ± 6	···	53 ± 4	700	1580	40.82	6.28	m
SDSS J014429.16−011047.3		0.0609	3600	29	68 ± 4	···	73 ± 12	70 ± 6	1760	2520	40.38	6.50	m
SDSS J015804.75−005221.9		0.0807	3600	34	49 ± 4	40 ± 3	47 ± 8	45 ± 3	1680	1180	40.56	5.90	m
SDSS J022756.28+005733.0		0.1280	3600	16	···	···	···	···	929	1040	41.60	6.25	m
SDSS J022849.51−090153.7		0.0724	5400	43	69 ± 3	···	57 ± 10	63 ± 5	697	720	40.39	5.38	m
SDSS J023310.79−074813.3	p	0.0312	1800	37	101 ± 7	114 ± 10	107 ± 4	107 ± 4	1740	1800	39.92	5.99	m
SDSS J024009.10+010334.5		0.1956	6300	16	···	···	···	···	737	580	41.64	5.75	m
SDSS J024402.24−091540.9		0.1220	5400	26	73 ± 9 :	79 ± 7	···	76 ± 6	970	1000	41.47	6.16	m
SDSS J024912.86−081525.6	gh02	0.0297	6000	22	49 ± 3	52 ± 2	60 ± 7	53 ± 3	843	702	40.31	5.32	b
SDSS J030417.78+002827.3		0.0450	2400	81	···	···	···	···	1000	900	41.50	6.08	m
SDSS J032515.59+003408.4	gh03	0.1023	3000	10	54 ± 6	47 ± 7	···	50 ± 5	970	886	41.31	5.98	b
SDSS J032707.32−075639.3	p	0.1537	3600	22	75 ± 6	···	···	75 ± 6	697	880	40.80	5.74	m
SDSS J034745.41+005737.2		0.1792	6600	19	107 ± 11	···	···	107 ± 11	865	4717	41.55	7.58	m
SDSS J074836.80+182154.2		0.0715	5400	28	40 ± 3	···	45 ± 8	42 ± 4	1660	1760	40.16	6.08	m
SDSS J080629.80+241955.6		0.0416	1200	28	73 ± 4	71 ± 5	69 ± 12	71 ± 5	918	1094	40.83	5.95	e
SDSS J080907.58+441641.4		0.0541	3600	23	66 ± 4	64 ± 3	···	65 ± 3	950	1104	40.78	5.94	b
SDSS J081550.23+250640.9		0.0726	3000	17	63 ± 3	67 ± 4	65 ± 5	65 ± 2	903	771	40.63	5.55	e
SDSS J082325.91+065106.4	p	0.0723	3600	9	55 ± 7	···	···	55 ± 7	1320	1300	39.93	5.70	m
SDSS J082347.95+060636.2	p	0.1037	3600	13	69 ± 9	···	···	69 ± 9	1480	1680	40.21	6.06	m
SDSS J082422.21+072550.4	p	0.0815	3600	6	···	···	···	···	1220	960	41.01	5.92	m
SDSS J082443.28+295923.5	p	0.0254	1800	47	100 ± 7	104 ± 4	118 ± 6	107 ± 3	871	691	40.35	5.33	e
SDSS J082912.67+500652.3	gh04	0.0436	2700	35	61 ± 4	62 ± 3	58 ± 4	60 ± 2	834	759	41.12	5.76	b
SDSS J083346.04+062026.6		0.1095	5400	26	39 ± 6	51 ± 5	···	45 ± 4	1070	640	40.72	5.42	m
SDSS J083928.45+082102.3		0.1302	3600	38	···	···	···	···	829	600	41.65	5.78	m
SDSS J084011.27+075915.7	p	0.1324	3600	11	···	···	···	···	1250	1060	41.09	6.04	m
SDSS J090320.97+045738.0		0.0567	5400	126	···	···	···	···	784	740	41.50	5.90	m
SDSS J090431.21+075330.8		0.0833	5400	89	···	···	···	···	938	860	41.29	5.94	m
SDSS J091032.80+040832.4	p	0.0732	5400	22	72 ± 12	···	···	72 ± 12	864	640	40.09	5.14	m
SDSS J091449.05+085321.1		0.1398	5400	41	···	···	···	···	849	720	41.68	5.96	m

Table 1—Continued

SDSS Name	Flag	z	Exp. (s)	S/N	σ(Mg Ib) (km s^{-1})	σ(Fe) (km s^{-1})	σ(Ca II) (km s^{-1})	σ_* (km s^{-1})	FWHM(Hα) GH07	FWHM(Hα) (km s^{-1})	log $L_{\rm H\alpha}$	log($M_{\rm BH}$)	Obs.
SDSS J092547.32+050231.6		0.1263	5400	22	···	···	···	···	760	580	41.55	5.71	m
SDSS J092700.53+084329.4		0.1124	5400	26	93 ± 12 :	107 ± 15	···	100 ± 10	1150	1220	41.29	6.26	m
SDSS J093147.25+063503.2	p	0.0853	5400	25	52 ± 9	···	···	52 ± 9	755	1460	41.00	6.29	m
SDSS J093147.25+063503.2	p	0.0857	3000	8	40 ± 8	39 ± 9	28 ± 12	35 ± 6	755	1360	41.00	6.22	e
SDSS J093829.38+034826.6		0.1193	5400	28	56 ± 7	···	···	56 ± 7	974	800	41.21	5.84	m
SDSS J094057.19+032401.2		0.0606	5400	210	82 ± 3	···	···	82 ± 3	908	800	41.45	5.95	m
SDSS J094310.12+604559.1	gh05	0.0743	3600	16	···	···	···	···	807	679	41.34	5.76	b
SDSS J094529.36+093610.4		0.0131	3600	81	75 ± 2	77 ± 3	···	76 ± 2	1930	1720	40.53	6.22	m
SDSS J095151.82+060143.7		0.0932	3600	35	70 ± 6	83 ± 10	···	76 ± 6	1260	660	41.01	5.58	m
SDSS J100035.47+052428.5		0.0785	2100	29	···	···	···	···	1000	940	41.62	6.17	m
SDSS J101108.40+002908.7	gh06	0.1002	1800	10	50 ± 7	61 ± 7	···	55 ± 5	1010	1083	41.36	6.18	b
SDSS J101627.32−000714.5	gh07	0.0950	3600	15	···	55 ± 7	···	55 ± 7	···	633	41.06	5.57	b
SDSS J102124.87+012720.3		0.0668	3600	36	78 ± 3	···	···	78 ± 3	1690	1600	40.39	6.09	m
SDSS J102348.44+040553.7	p	0.0988	5400	27	91 ± 13	···	···	91 ± 13	696	520	40.95	5.34	m
SDSS J103518.74+073406.2		0.0674	5400	55	109 ± 4	···	···	109 ± 4	867	800	41.27	5.87	m
SDSS J104210.03−001814.7		0.1144	5400	32	···	···	···	···	816	800	41.64	6.04	m
SDSS J105755.66+482502.0		0.0732	1200	22	50 ± 3	49 ± 4	38 ± 3	45 ± 2	957	898	40.62	5.68	e
SDSS J110501.97+594103.6		0.0337	900	50	124 ± 5	125 ± 8	120 ± 19	123 ± 7	702	3672	40.51	6.89	e
SDSS J110540.46+035309.0		0.0993	3600	47	···	···	···	···	820	800	41.62	6.03	m
SDSS J111031.61+022043.2		0.0799	5400	92	78 ± 3	76 ± 4	···	77 ± 3	1000	920	41.39	6.05	m
SDSS J111749.17+044315.5		0.1082	5400	36	62 ± 9 :	76 ± 6	···	69 ± 5	826	680	41.38	5.77	m
SDSS J112526.51+022039.0		0.0490	5400	136	91 ± 2	···	83 ± 10	87 ± 5	1090	940	41.14	5.96	m
SDSS J114339.49−024316.3		0.0937	5400	61	97 ± 8	98 ± 5	···	97 ± 5	919	1460	41.18	6.37	m
SDSS J114343.76+550019.3	p	0.0272	1800	22	31 ± 3	31 ± 3	32 ± 3	31 ± 2	1070	1393	40.39	5.97	e
SDSS J114439.34+025506.5	p	0.1018	5400	21	48 ± 4	47 ± 6	···	47 ± 4	942	720	40.51	5.43	m
SDSS J114633.98+100244.9		0.1245	5400	31	···	62 ± 8	···	62 ± 8	790	780	41.54	5.97	m
SDSS J115138.24+004946.4	gh09	0.1950	1200	13	···	···	···	···	810	1304	41.74	6.52	e
SDSS J121518.23+014751.1		0.0713	5400	95	74 ± 4	···	88 ± 4	81 ± 3	910	1000	41.08	5.99	m
SDSS J122342.81+581446.1		0.0146	1800	29	44 ± 3	47 ± 3	46 ± 3	45 ± 2	979	1577	40.30	6.04	e
SDSS J124035.81−002919.4	gh10	0.0812	1800	26	49 ± 5	63 ± 6	58 ± 7	56 ± 3	915	713	41.64	5.93	b
SDSS J125055.28−015556.6	gh11	0.0815	1800	18	68 ± 5	68 ± 8	64 ± 8	66 ± 4	···	2266	41.27	6.80	b
SDSS J131310.12+051942.1		0.0492	5400	76	68 ± 3	···	80 ± 4	74 ± 3	888	580	40.68	5.32	m
SDSS J131310.12+051942.1		0.0489	1200	16	64 ± 5	65 ± 5	68 ± 6	65 ± 3	888	645	40.68	5.41	e
SDSS J131651.29+055646.9		0.0554	5400	101	82 ± 3	···	···	82 ± 3	1260	980	41.04	5.95	m

Table 1—Continued

SDSS Name	Flag	z	Exp. (s)	S/N	σ(Mg Ib) (km s^{-1})	σ(Fe) (km s^{-1})	σ(Ca II) (km s^{-1})	σ_* (km s^{-1})	FWHM(Hα) GH07	FWHM(Hα) (km s^{-1})	log $L_{\rm H\alpha}$	log($M_{\rm BH}$)	Obs.
SDSS J131659.37+035319.8	p	0.0459	5400	36	82 ± 6	···	80 ± 12	81 ± 7	887	880	40.61	5.66	m
SDSS J131926.52+105610.9		0.0647	5400	174	47 ± 3	···	···	47 ± 3	840	860	41.10	5.86	m
SDSS J134144.51−005832.9		0.1476	5400	31	···	···	···	···	835	660	41.39	5.75	m
SDSS J141234.67−003500.0	gh13	0.1269	1800	16	···	···	···	···	884	945	41.56	6.15	b
SDSS J143450.62+033842.5	gh14	0.0284	1800	17	46 ± 6	63 ± 3	63 ± 6	57 ± 3	1050	1001	40.34	5.65	b
SDSS J144052.60−023506.2		0.0448	5400	143	···	···	73 ± 8	73 ± 8	950	840	41.21	5.89	m
SDSS J144705.46+003653.2		0.0953	5400	44	63 ± 4	65 ± 7	···	64 ± 4	1160	1500	40.96	6.29	m
SDSS J145045.54−014752.8		0.0996	5400	61	131 ± 6	145 ± 10	···	138 ± 6	955	2420	41.49	6.96	m
SDSS J150754.38+010816.7		0.0613	5400	114	131 ± 5	···	133 ± 3	132 ± 3	699	1680	40.40	6.14	m
SDSS J153425.59+040806.7		0.0395	2200	7	···	···	···	···	927	449	40.02	4.79	e
SDSS J154257.49+030653.2		0.0655	5400	117	···	···	···	···	1070	980	41.41	6.12	m
SDSS J155005.95+091035.7		0.0916	5400	51	80 ± 10	77 ± 8	···	78 ± 6	835	1100	41.10	6.08	m
SDSS J161227.84+010159.7		0.0973	7200	70	···	···	···	···	944	920	41.40	6.05	m
SDSS J161751.98−001957.4		0.0573	5100	14	65 ± 6	···	···	65 ± 6	1120	1020	40.37	5.68	m
SDSS J162403.63−005410.3		0.0468	5400	35	94 ± 4	···	···	94 ± 4	1150	1340	40.64	6.05	m
SDSS J162636.40+350242.0		0.0342	1800	34	48 ± 2	53 ± 2	56 ± 2	52 ± 1	802	714	40.76	5.54	e
SDSS J163159.59+243740.2		0.0436	2900	38	63 ± 3	61 ± 3	74 ± 4	66 ± 2	839	541	40.84	5.33	e
SDSS J170246.09+602818.9	gh16	0.0692	1100	18	···	81 ± 11	82 ± 9	81 ± 7	···	1116	41.25	6.16	b
SDSS J172759.15+542147.0	gh17	0.0997	3500	17	···	67 ± 8	···	67 ± 8	806	656	41.27	5.68	b
SDSS J205822.14−065004.3		0.0742	5400	62	58 ± 3 :	···	···	58 ± 3	917	860	41.54	6.06	m
SDSS J213728.62−083823.3		0.1609	7200	36	···	···	···	···	904	1000	41.76	6.29	m
SDSS J215658.30+110343.1		0.1081	3600	36	88 ± 8	···	···	88 ± 8	···	990	42.14	6.45	b
SDSS J221139.16−010535.0		0.0925	7200	20	69 ± 10	68 ± 11	···	68 ± 7	1070	1540	40.95	6.31	m
SDSS J230649.77+005023.4		0.0610	3600	39	58 ± 3	···	73 ± 6	65 ± 3	1800	1479	40.55	6.10	m
SDSS J232159.06+000738.8	gh18	0.1840	3600	12	76 ± 9	···	···	76 ± 9	···	1531	41.52	6.56	b
SDSS J233837.10−002810.3	gh19	0.0357	3600	26	58 ± 3	56 ± 2	55 ± 3	56 ± 2	···	1553	40.06	5.92	b
SDSS J234807.14−091202.6		0.0779	5400	34	80 ± 7	···	···	80 ± 7	1490	1480	40.76	6.19	m

Note. — Object names are given by their SDSS coordinate designations. Those names in Greene & Ho (2004) are also given. Objects with "possible" broad Hα are indicated as "p". S/N is the mean signal-to-noise ratio per pixel in the spectrum in the spectral region around or redward of Mg Ib used to measure σ_*. For MagE data, if the Mg Ib fitting region and Fe fitting region are on the same echelle order, we measure σ_* from one region extending across these two, and list the result as σ(Mg Ib). The σ_* with ":" is dubious due to limited numbers of fitting templates. The FWHM(Hα)$_{GH07}$ and $L_{\rm H\alpha}$ values are from GH07 if available and otherwise from Greene & Ho (2004). For SDSS

J215658.30+110343.1, we use L_{5100} from Barth et al. (2005) and the L_{5100}-$L_{\mathrm{H}\alpha}$ relation in Greene & Ho (2005b) to estimate $L_{\mathrm{H}\alpha}$. Virial mass estimates of M_{BH} are in units of $M_{\odot}$. The observational sub-samples are indicated as b, e and m for ESI sample in Barth et al. (2005), new ESI observation and new MagE observation, respectively.

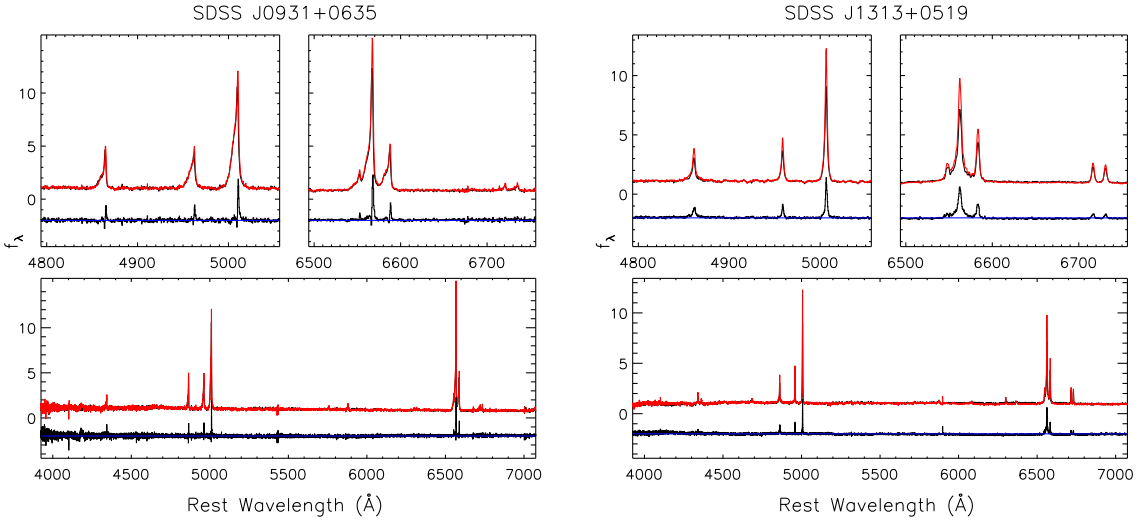


Fig. 1.— Comparison of MagE and ESI spectra (in black and red, respectively) for SDSS J093147.25+063503.2 and SDSS J131310.12+051942.1. The ESI data have been rebinned to the spectral resolution of the MagE data. To facilitate comparison, all spectra have been rescaled to have flux density of unity at 5100 Å. In each panel, the residual from subtraction of the MagE spectrum from the ESI spectrum (minus an arbitrary constant for clarity) is shown as a black line in the bottom. The blue horizontal line shows the arbitrary constant.

Table 2. Regression parameters

Sample (1)	N (2)	Uncert. (3)	α (4)	β (5)	ϵ_0 (6)
Full	155	1σ	7.68 ± 0.08	3.32 ± 0.22	0.46 ± 0.03
Full	155	3σ	7.69 ± 0.08	3.28 ± 0.22	0.28 ± 0.05
Full w/o "p"	142	1σ	7.75 ± 0.08	3.48 ± 0.21	0.41 ± 0.03

Note. — Col. (1): Data set considered; the "Full" sample comprises objects with both $M_{\rm BH}$ and σ_* available, including the SDSS sample and 24 RM AGNs with stellar velocity dispersion measurements presented by Woo et al. (2010), NGC 4395 and POX 52. The "Full w/o p" subsample denotes the full sample minus the objects classified as having possible broad Hα. Col. (2): Number of objects in each sample. Col. (3): Adopted uncertainties for $M_{\rm BH}$. Col. (4): Zero point assuming $\log M_{\rm BH} = \alpha + \beta \log(\sigma_*/200 \text{ km s}^{-1})$, for $f = 0.75$. Col. (5): $M_{\rm BH} - \sigma_*$ slope. Col. (6): intrinsic scatter.

Table 3. Regression parameters for barred / unbarred disk galaxies

		Free fit			Fit with fixed slope		
Sample (1)	N (2)	α (3)	β (4)	ϵ_0 (5)	α (6)	β (7)	ϵ_0 (8)
Disk	63	7.50 ± 0.13	3.04 ± 0.30	0.43 ± 0.05	7.96 ± 0.07	4.24	0.50
Barred	25	7.81 ± 0.27	4.13 ± 0.72	0.46 ± 0.09	7.86 ± 0.09	4.24	0.40
Unbarred	38	7.44 ± 0.15	2.79 ± 0.34	0.42 ± 0.06	8.04 ± 0.09	4.24	0.54
Disk w/o "p"	56	7.56 ± 0.13	3.19 ± 0.31	0.42 ± 0.05	7.95 ± 0.07	4.24	0.46
Barred w/o "p"	22	7.80 ± 0.29	4.03 ± 0.80	0.46 ± 0.09	7.87 ± 0.09	4.24	0.40
Unbarred w/o "p"	34	7.52 ± 0.15	3.01 ± 0.33	0.40 ± 0.06	8.01 ± 0.09	4.24	0.48

Note. — Col. (1): Data set considered; the "Disk" ("Barred" / "Unbarred") sample comprises the "Full" sample with morphological type available and classified as (barred / unbarred) disk galaxies. The "Disk w/o p" subsample denotes the "Disk" sample minus the objects classified as having "possible" broad Hα. Col. (2): Number of objects in each subsample. Col. (3): Zeropoint assuming $\log M_{\rm BH} = \alpha + \beta \log(\sigma_*/200 \text{ km s}^{-1})$, for $f = 0.75$. Col. (4): $M_{\rm BH} - \sigma_*$ slope. Col. (5): Intrinsic scatter. Col. (6): Zeropoint of $M_{\rm BH} - \sigma_*$ relation with the slope fixed to that of inactive galaxies listed in Col.(7), and the upper limits on intrinsic scatter listed in Col. (8).

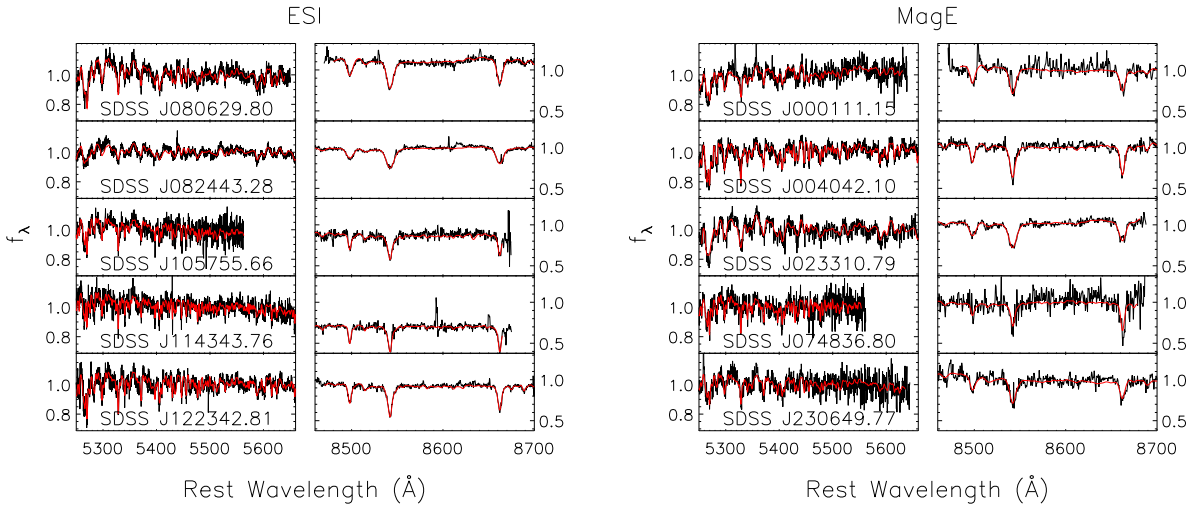


Fig. 2.— Examples of ESI (left) and MagE (right) spectra of spectra in the Fe and CaT regions. The spectra are flux-calibrated in f_λ units and normalized to a flux level of unity. The observed spectrum is in black and the best-fitting broadened stellar template is in red.

Table 4. Regression parameters for different disk inclination

			Free fit			Fit with fixed slope		
Sample (1)	axis ratio (2)	N (3)	α (4)	β (5)	ϵ_0 (6)	α (7)	β (8)	ϵ_0 (9)
High	$b/a < 0.72$	20	7.42 ± 0.25	3.24 ± 0.70	0.50 ± 0.10	7.74 ± 0.11	4.24	0.48
Medium	$0.72 < b/a < 0.88$	20	7.70 ± 0.20	3.86 ± 0.49	0.38 ± 0.10	7.85 ± 0.09	4.24	0.36
Low	$b/a > 0.88$	15	7.59 ± 0.32	2.76 ± 0.67	0.44 ± 0.12	8.25 ± 0.13	4.24	0.48

Note. — Col. (1): Data set considered; the "High" ("Medium" / "Low") sample comprises the "Disk" sample with the axis ratio of the disk component available, divided into three bins of inclination angle. Col. (2): axis ratio range of each subsample. Col. (3): Number of objects in each subsample. Col. (4): Zeropoint assuming $\log M_{\rm BH} = \alpha + \beta \log(\sigma_*/200 \text{ km s}^{-1})$, for $f = 0.75$. Col. (5): $M_{\rm BH} - \sigma_*$ slope. Col. (6): Intrinsic scatter. Col. (7): Zeropoint of $M_{\rm BH} - \sigma_*$ relation with the slope fixed to that of inactive galaxies listed in Col.(8), and the upper limits on intrinsic scatter listed in Col. (9).

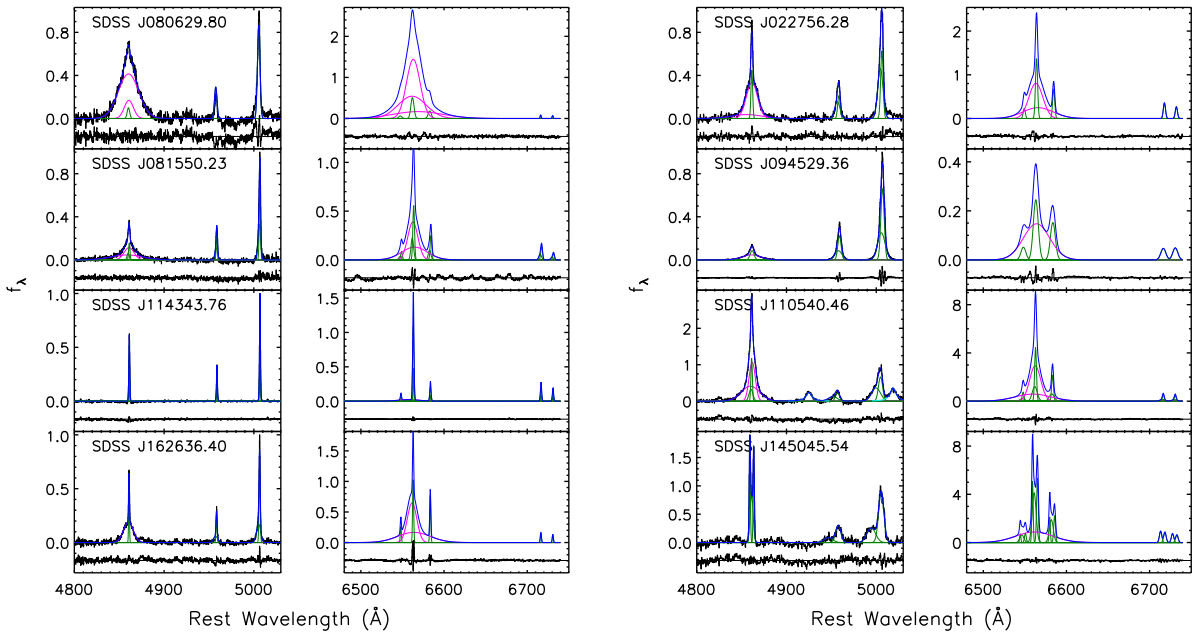


Fig. 3.— Examples of fitting to the Hβ + [O III] and Hα+[N II] regions for ESI (left) and MagE (right) data. The spectra are flux-calibrated in f_λ units and arbitrarily normalized to a flux level of unit around the peak of [O III] λ5007 Å. In each panel, continuum-subtracted spectra (black) and the best-fit model (blue) are shown, with their residuals shifted downward by an arbitrary constant for clarity. Individual components are overplotted: narrow lines (green), broad lines (magenta) and Fe II emission (cyan) if present.

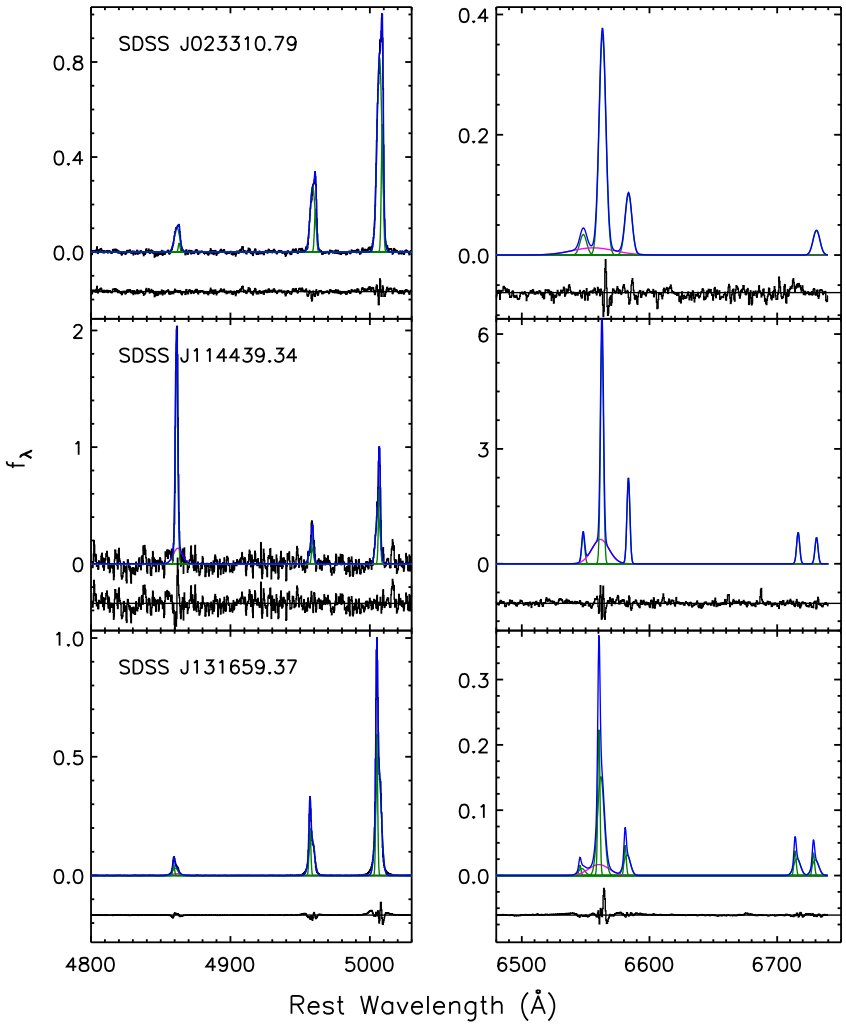


Fig. 4.— Examples of galaxies showing possible broad Hα components. Fit components are illustrated as in Figure 3.

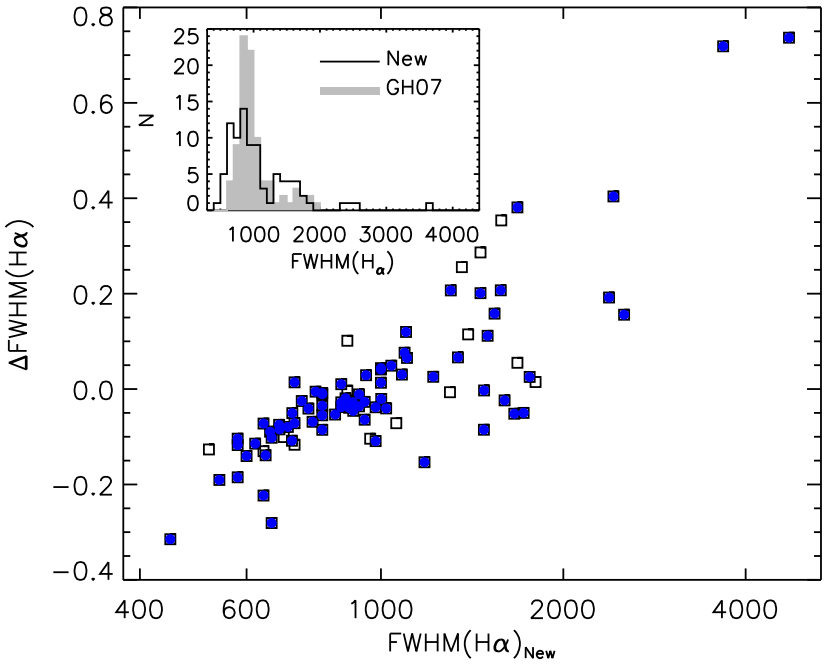


Fig. 5.— ΔFWHM(Hα), the logarithmic difference between the GH07 measurement of broad Hα FWHM and our new measurement, as a function of broad Hα linewidth. Filled and open squares represent galaxies with definite and possible broad Hα, respectively. The inset box shows the distributions of broad Hα linewidths from GH07 and from our new measurements.

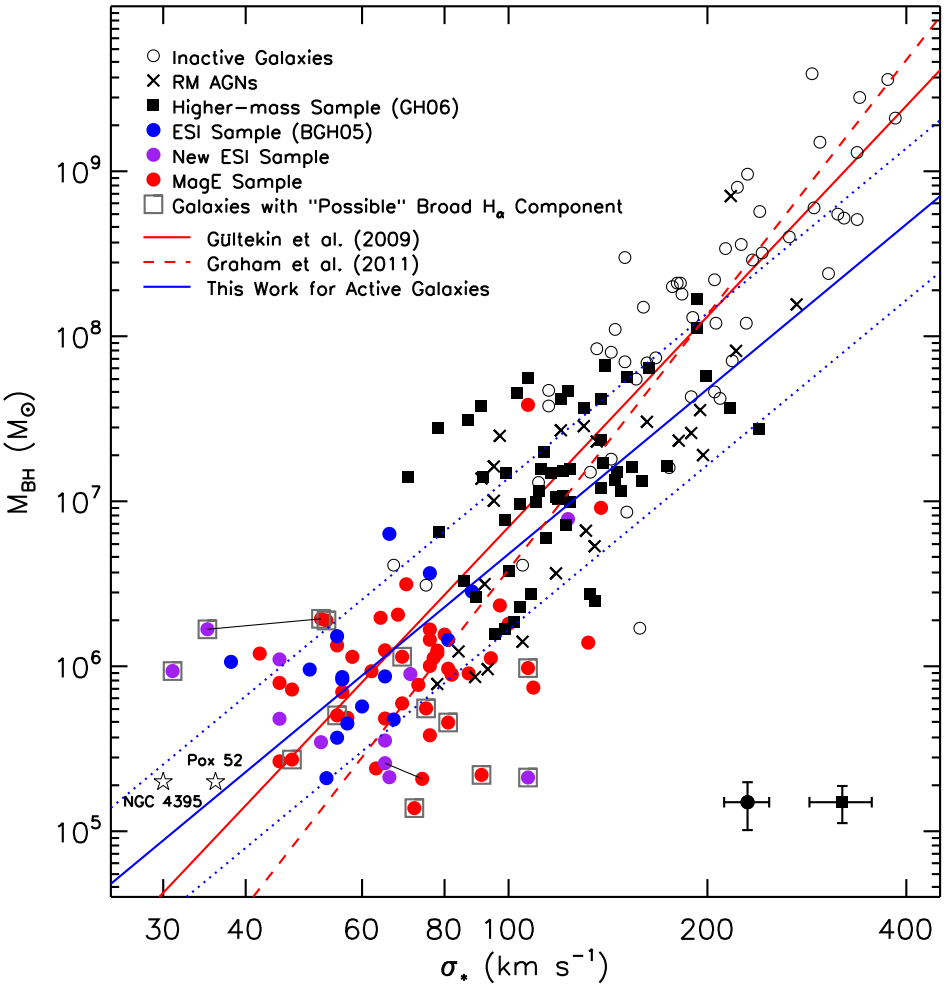


Fig. 6.— The $M_{\rm BH}-\sigma_*$ relation for massive black holes. Filled dots represent new measurements from this work. Red dots are the MagE sample, purple dots are the newly observed ESI objects, and blue dots are the objects originally from the BGH05 sample. For objects observed with both ESI and MagE, both measurements are shown, connected by a short black line. The filled dots over-plotted with grey squares represent the galaxies with "possible" broad Hα components. Filled squares represent the 56 higher-mass active galaxies selected from SDSS by Greene & Ho (2006b), with BH masses updated with Equation 6. Crosses represent literature data of 24 RM AGNs with stellar velocity dispersion measurements presented by Woo et al. (2010). NGC 4395 and POX 52 (Filippenko & Ho 2003; Peterson et al. 2005; Thornton et al. 2008) are illustrated with stars. All the $M_{\rm BH}$ are scaled to the virial factor of $f = 0.75$ or $f_\sigma = 3$, in the virial mass $M_{\rm BH} = fR_{\rm BLR}\Delta V^2/G$ (see text for details). Open circles represent objects with dynamically determined BH masses compiled by Gültekin et al. (2009), and the red line is the $M_{\rm BH}-\sigma_*$ relation derived by Gültekin et al. (2009). Red dashed-line is the $M_{\rm BH}-\sigma_*$ relation reported by Graham et al. (2011). The blue solid line shows our best-fit $M_{\rm BH}-\sigma_*$ relation for active galaxies with $\alpha = 7.68 \pm 0.08$ and $\beta = 3.32 \pm 0.22$, and the blue dotted lines show the intrinsic scatter

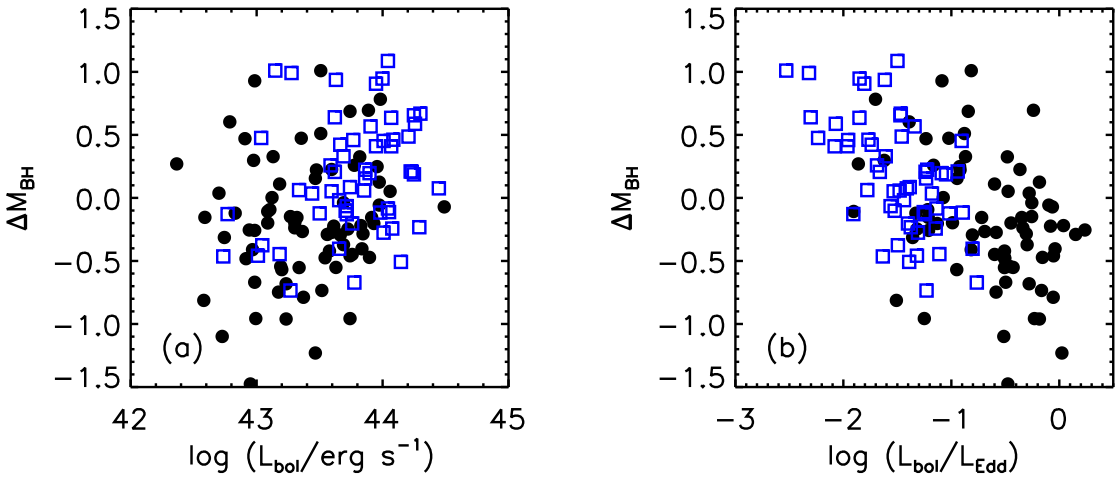


Fig. 7.— The $M_{\rm BH} - \sigma_*$ residual, $\Delta M_{\rm BH} \equiv \log(M_{\rm BH}/M_\odot) - \log(M_{\rm BH}/M_\odot)_{\rm fit}$ vs. (a) bolometric luminosity, (b) $L_{\rm bol}/L_{\rm Edd}$. Filled dots are the low-mass sample in this work. Blue squares are those 56 active galaxies selected from SDSS by Greene & Ho (2006b), with BH masses updated with Equation 6.

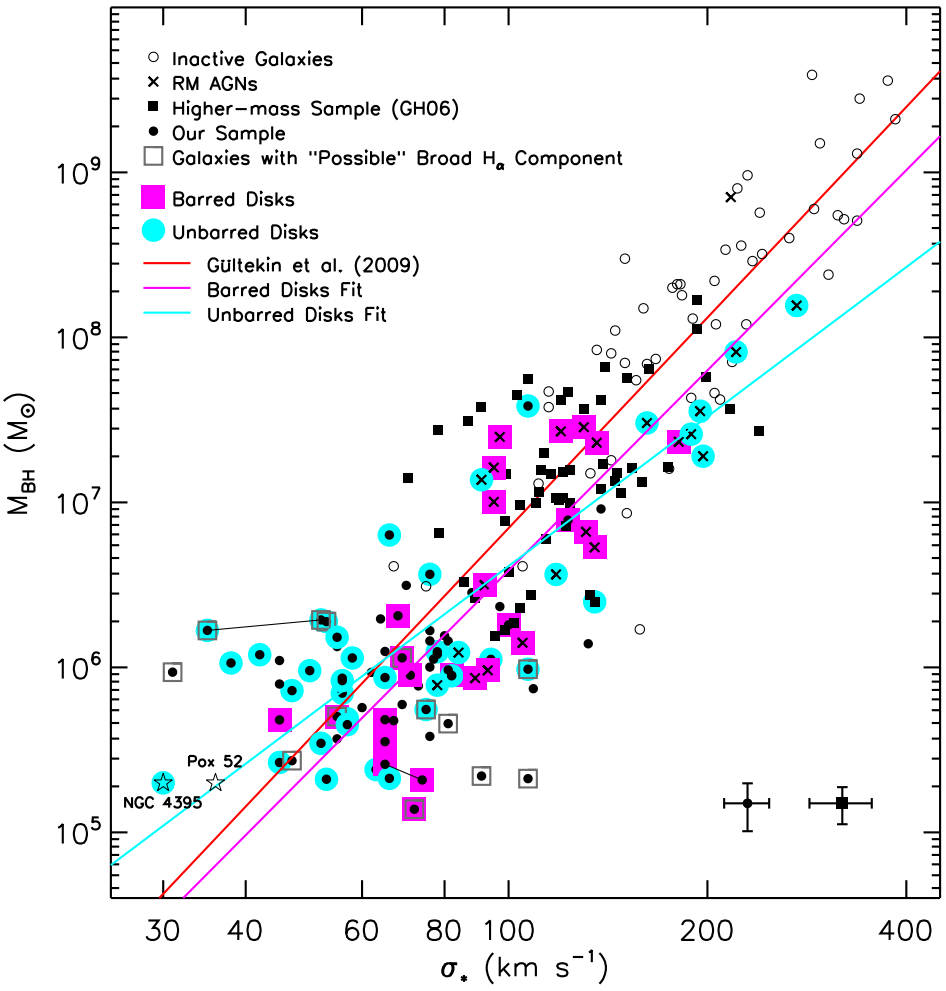


Fig. 8.— The same as Figure 6, with the morphological classification of barred and unbarred disk galaxies shown. Small filled circles represent our sample with low-mass $M_{\rm BH}$. Large magenta filled squares represent barred disk galaxies, while the cyan circles denote unbarred disks. Magenta and cyan lines show the best-fitting $M_{\rm BH} - \sigma_*$ relation for the barred and unbarred subsamples that excludes the p objects with uncertain detections of broad Hα, respectively.

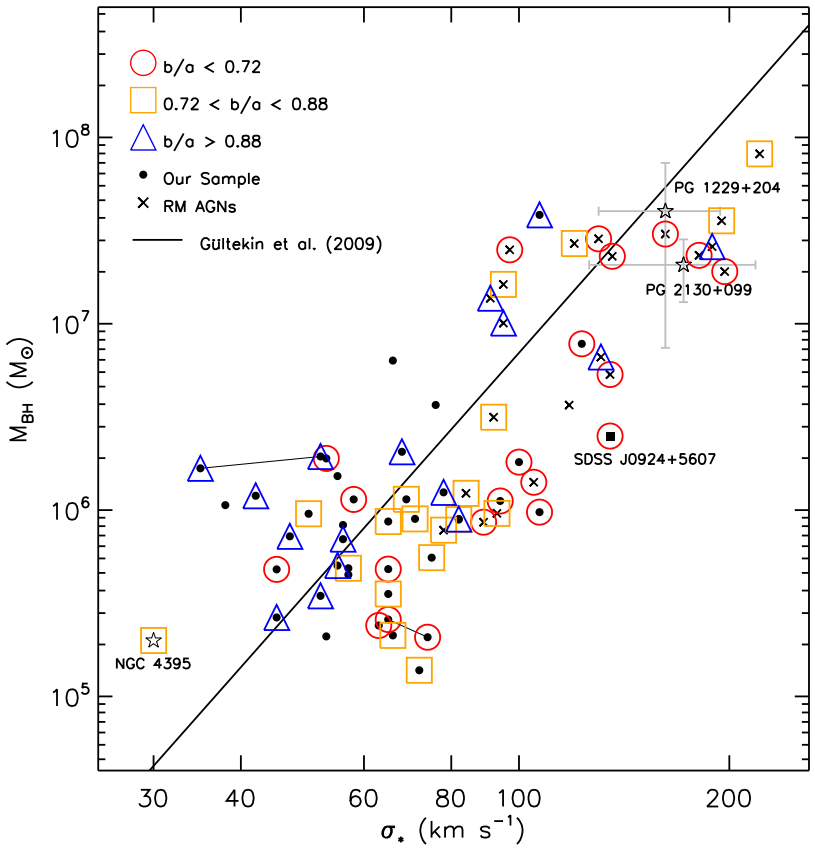


Fig. 9.— The same as Figure 6, enlarged to highlight the active galaxies classified as disk galaxies. Small filled circles, squares and crosses represent the same as Figure 6. Three subsamples of high-, medium- and low-inclination objects are overplotted with red open circles, orange open squares and blue triangles, respectively. The $M_{\rm BH} - \sigma_*$ relation from Gültekin et al. is shown for comparison. Only one galaxy (SDSS J0924+5607) from the GH06 higher-mass SDSS sample is observed in the *HST* imaging survey. Two extra PG objects are also shown as stars. For PG 1229+204 and PG 2130+099, the BH masses are $4.0 \times 10^7 M_\odot$ and $2.1 \times 10^7 M_\odot$ (virial product from Peterson et al. 2004; Grier et al. 2008) under the assumption of $f_\sigma = 3$ as discussed in §4.2, and velocity dispersion are 162 ± 32 km s^{-1} and 172 ± 46 km s^{-1} (Dasyra et al. 2007), respectively. Their axis ratios of disk components are 0.62 and 0.55, respectively, and they are classified as high-inclination objects.

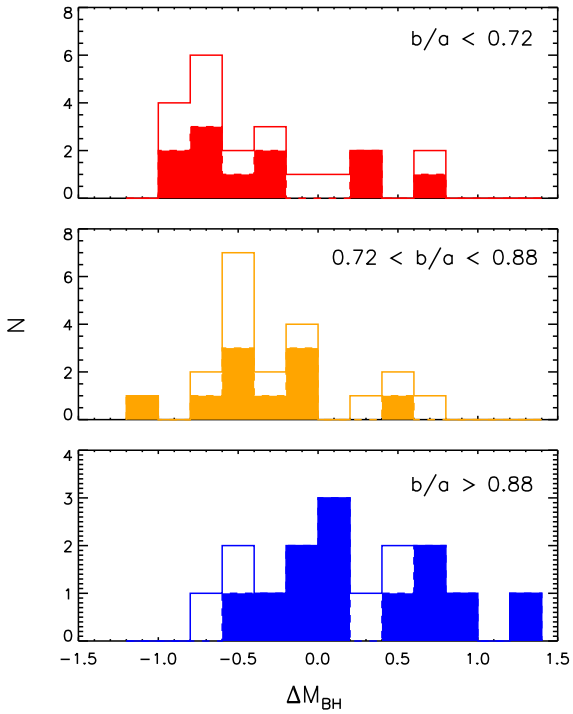


Fig. 10.— Distribution of $\Delta M_{\rm BH}$ defined as the $M_{\rm BH}$ deviation from the best-fit $M_{\rm BH} - \sigma_*$ relation from Gültekin et al., in three bins of disk inclination with the axis ratio range shown at the top right in each panel. From top to bottom is high- (close to edge-on), medium- and low-inclination (close to face-on). In each panel, the open and filled histograms show the distributions for all AGNs having host galaxy axis ratios (including the reverberation-mapped objects) and the subset from only our SDSS sample, respectively.

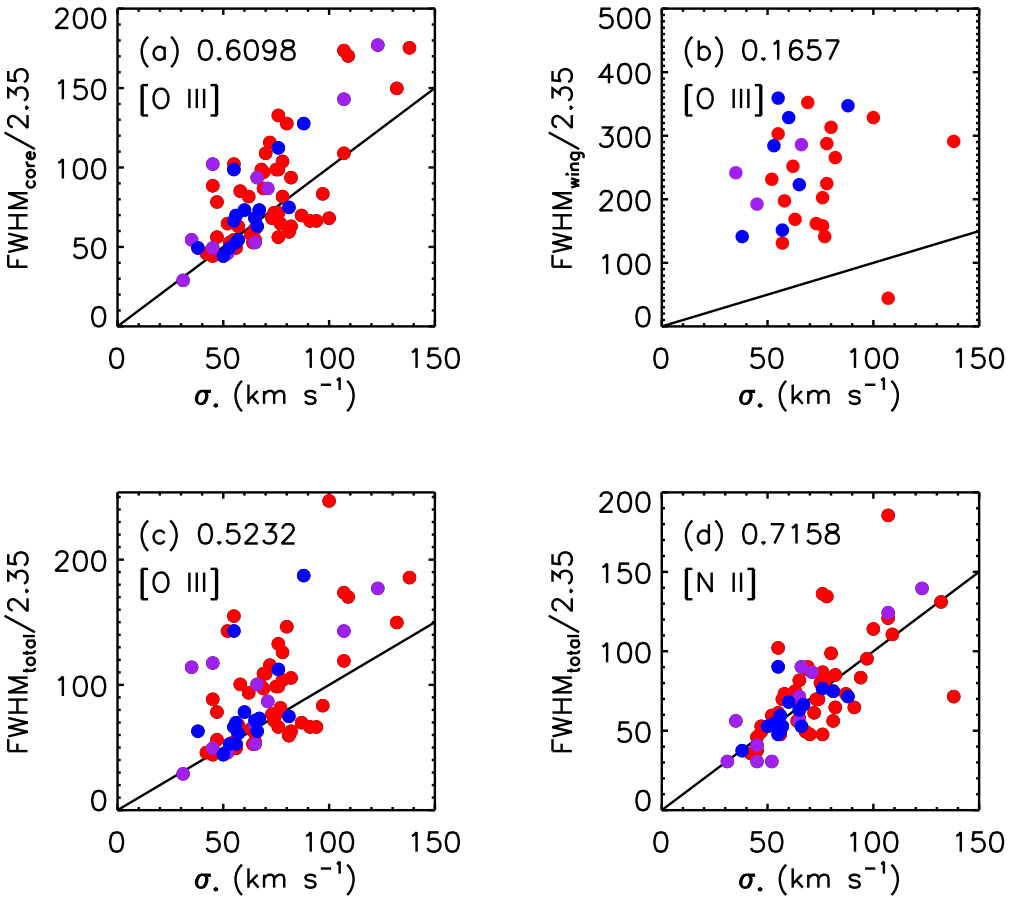


Fig. 11.— FWHM/2.35 vs. σ_* for: (a) the core component of [O III] after removing the shifted wing component; (b) the blue-shifted or red-shifted wing component of [O III]; (c) the overall profile of [O III]; and (d) the overall profile of [N II]. The colors of plot symbols are as in Figure 6. The number at the top of each panel gives the Spearman rank correlation coefficient for the plotted data. The solid line in each panel represents FWHM/2.35 = σ_*.

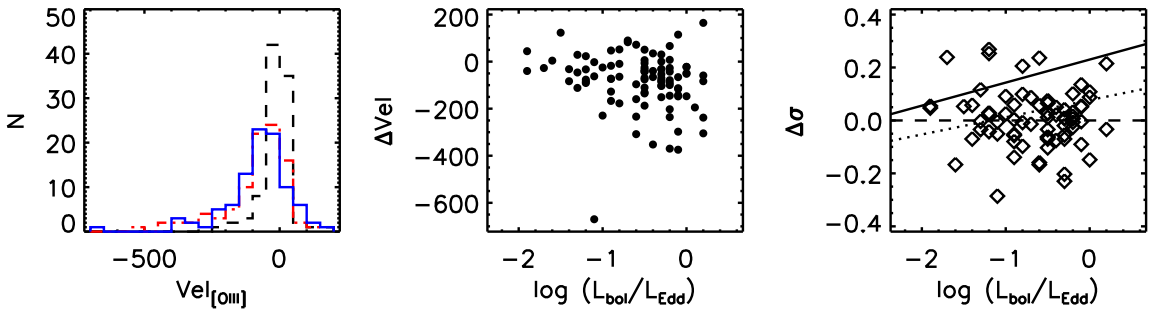


Fig. 12.— *Left panel*: Distribution of velocity shifts relative to the stellar absorption system for the core component (black dashed) and the wing component (red dot-dashed) of [O III]; Distribution of ΔVel (km s^{-1}), defined to be the relative velocity-shift between the wing to core components, is shown in blue solid histogram. *Middle panel*: ΔVel as a function of Eddington ratio. The object with $|\Delta\mathrm{Vel}| > 600$ km s^{-1} is SDSS J145045.54−014752.8, showing obvious double-peaked features in narrow lines. *Right panel*: Distribution of the residuals $\Delta\sigma \equiv \log\sigma_g - \log\sigma_*$ ($\sigma_g \equiv \mathrm{FWHM}/2.35$) versus Eddington ratio, L_{bol}/L_{Edd}, for [N II] λ6583 Å. The dashed line denotes $\sigma_g = \sigma_*$. The solid and dotted lines show the relations found by Ho (2009, Equation 3) and Greene & Ho (2005a, Equation 4).

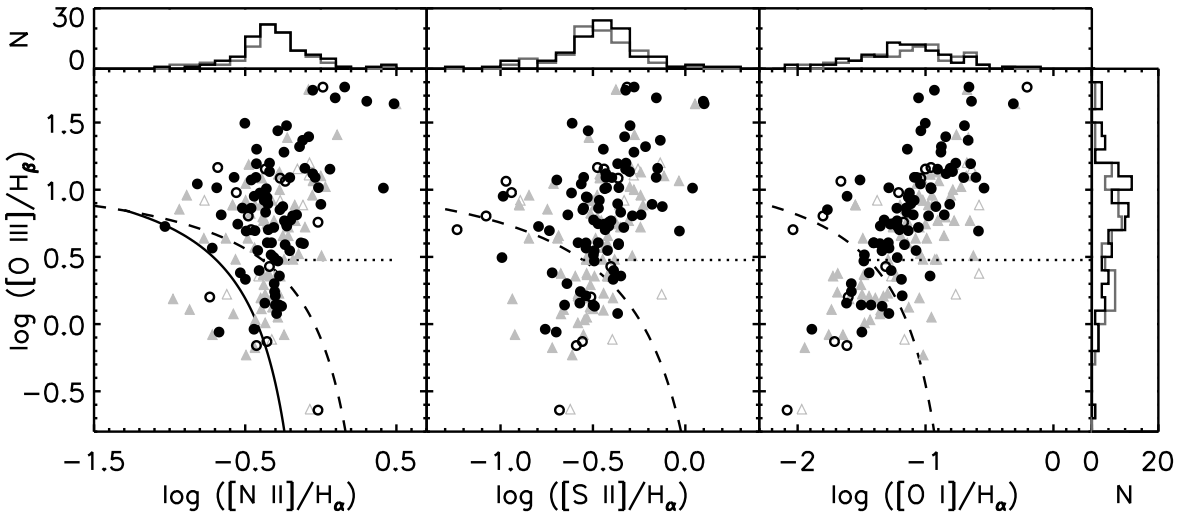


Fig. 13.— Diagnostic diagrams for [O III]/Hβ vs. [N II]/Hα, [S II]/Hα and [O I]/Hα. Filled circles represent objects with definite broad Hα, and open circles represent objects classified as having possible broad Hα. Grey triangles show the line ratios measured from the SDSS data by GH07 (open triangles represent their candidate sample). Dashed curves are the maximum starburst lines from Kewley et al. (2006); the solid curve is the pure star formation boundary (Kauffmann et al. 2003); The horizontal dotted line marks [O III]/Hβ= 3.